

Self-equilibrated residual based error estimation on 1-irregular meshes in finite elasticity

W. RACHOWICZ¹⁾, A. ZDUNEK²⁾

 $^{1)} Cracow\ Univesity\ of\ Technology,\ Cracow,\ Poland,\ e-mail:\ wrachowicz@pk.edu.pl$

We consider well-established techniques for the residual error estimation of finite element approximations applied to problems in finite elasticity. The element implicit residual method and the method of self-equilibration are applied to nearly incompressible and anisotropic finite strain elastic cases. Our contribution regarding the residual error estimation concerns generalising the approach to 1-irregular meshes. That is, we recover equilibrating element tractions in the presence of compatibility enforcing constraints. The generalisations are illustrated using numerical experiments. The considered variants of the estimators are compared.

Key words: error estimation, finite element approximation, finite elasticity, residual, self-equilibrated.



Copyright © 2025 The Authors.

Published by IPPT PAN. This is an open access article under the Creative Commons Attribution License CC BY 4.0 (https://creativecommons.org/licenses/by/4.0/).

1. Motivation

THE ASSESSMENT OF THE RELIABILITY OF A FINITE ELEMENT SOLUTION which models a real problem plays a crucial role in many areas of mechanics. In Linear Fracture Mechanics (LFM) prediction of crack-growth is central. In LFM stressintensity functions with high accuracy are required. In this particular case the strength and the location of the stress singularity is known. The necessary accuracy of the displacement solution to the governing Navier-Lamé linear elasticity boundary value problem can then be obtained using a suitable a priori strongly graded mesh enclosing the crack-tip – in one shot. That is, without any error estimation followed by hp-adaptivity. Moreover, in LFM simultaneous multi-crack scenarios in huge problems can be studied reliably using the so-called splitting method [1], due to the superposition principle. Huge reliable databases of stressintensity functions are created using this approach. These databases are used to determine the service life of aircraft [2]. The global problem is solved using the massively parallelized code STRIPE [3], with the multi-level domain decomposition (DD) solver [4] which is extremely efficient for a coercive problem. The local, not intrusive problems, are solved massively in parallel aside. Both strides are run on some of todays' most powerful computers. The methodology has reached a high level of technical readiness level (TRL) and it is mature.

²⁾ HB BerRit, Solhelmsbackarna 73, Spanga, Sweden

Without the superposition principle, and without guaranteed coerciveness, the situation changes drastically. The issue of computing finite element approximations reliably for large scale problems in geometric nonlinear elasticity is a challenge [5]. For an account in stiffened shell-like aeronautic structures, see [6]. It becomes evident tackling problem with complex instabilities [7] and even more modelling finite strains [8]. The discretization errors we are considering here, are mainly not caused by strong singularities, as opposed to the situation in LFM. Instead, the solution, the displacement fields may rapidly change character with the load level. Especially in cases with local loss of stability [7]. For large scale problems, the use of a sufficiently fine homogeneous mesh will generally be impossible and inefficient, and it may be impossible to construct a priori a strongly graded mesh to cover the evolution 1.

Therefore, to compute a solution in *finite elasticity* with the desired accuracy we use self-equilibrated residual based error estimates on 1-irregular meshes and mark candidate elements allowing for 1-irregular h-refinement. (By 1-irregularity we understand the situation when we divide selected elements preserving the principle that the ratio of sizes of neighboring elements cannot exceed 1:2, i.e., the larger hexahedral element has 4 smaller element-neighbors across its face or 2 across the edge. Compatibility of approximation is enforced through multipoint constraints). The procedure will typically be repeated in several steps for each load-increment of the Newton-Raphson method used. Solving the incremental linearised problems we can in fact use a DD-solver. The DD part, deciding which subdomains are subject to error estimation and adaptivity and which are fixed, is outside the scope of this study. For simplicity, here we use a onelevel DD [9-11], applying error estimation and adaptivity to all subdomains. As a consequence, the whole tangent stiffness has to be factored again as soon as an element is divided or its polynomial degree is changed. On the other hand, full hp-adaptivity using 1-irregular h-subdivisions and anisotropic p-enrichments is in our hands using the 3Dhp code, described in the textbooks [12, 13].

The state-of-the-art of a posteriori error estimation in the finite element analysis is captured in the textbooks [14–16] and in the review article [17].

The main focus of this study is the estimation of the local discretization error in the displacements, using *implicit a posteriori residual based estimators*, proposed by Ainsworth and Oden [18] and improved by Ladevéze and Maunder [19]. The main advantage of these estimates is that they do not involve the polynomial-order dependent constants.

Rachowicz [20] generalised this approach for 3D 1-irregular h-subdivisions of hexahedra and linear elliptic boundary value problems. This estimation technique was applied for linear steady-state Maxwell's scattering problems by

¹Needless to say, knowledge about corners holes etc. is used in the nominal meshing.

ZDUNEK and RACHOWICZ in [21]. The method of Ainsworth and Oden was generalised for 3D 1-irregular meshes of triangular prisms by ZBOIŃSKI [22].

AINSWORTH and ODEN [14] pointed out that their error estimation technique without polynomial-order dependent constants is generalisable to non-linear problems and provided some examples [14, Section 9.4]. Brink and Stein [23] generalised the technique to nearly incompressible large strain elasticity introducing a Helmholtz decomposition of the first Piola–Kirchhoff stress. Later Rüter and Stein [24] applied this idea to transverse isotropic finite elasticity. So far these error estimates were used applying regular h-refinements to regular meshes. The generalisation of the error estimation technique on 1-irregular meshes allowing for 1-irregular h-refinements in finite elastic problems with 1- and 2-fibre family reinforcements were considered by ZDUNEK and RACHOWICZ [25] and [8].

In this contribution we use and evaluate two implicit a posteriori error estimation methods applied to problems in finite elasticity; namely the method of Demkowicz et al. [26] and the approach with self-equilibration of residuals due to Ainsworth and Oden [18]. The self-equilibration has the advantage that one can solve local purely Neumann problems, on the element level and it is free from polynomial-order-dependent constants. The equilibration procedure will be considered in two variants, the first, due to Ainsworth and Oden [27], and the second, due to Ladevéze and Maunder [19], which we generalized to 3D 1-irregular meshes.

We compare the error estimates for representative examples of isotropic incompressible and anisotropic finite elasticity. We investigate whether estimated element errors of these techniques demonstrate a common growth of value as this is necessary for adaptivity of meshes.

In view of the discussion in the introduction, 3D finite element codes using 1-irregular automatically generating adaptive meshes in finite elasticity are rare. They are also necessary since sources of errors change with finite deformations, directions of reinforcing fibres. Other applications may involve the point of contact or the line of necking, etc.

It is also confirmed that such codes are developed in leading scientific institutions, see BADGER *et al.* [28], allowing one to solve problems of the size 10^9 degrees-of-freedom on adaptive meshes².

The rest of paper is organised as follows. In Section 2 the mixed finite element formulation for nearly incompressible materials in finite elasticity is presented. In Section 3.1 the idea to use a Helmholtz decomposition of the first Piola–Kirchhoff stress in error estimation [23, 24] is summarised. In Section 3 also the *a posteriori* implicit error estimation methods we employ are presented. The one by

 $^{^2}$ This is a newer version of 3Dhp on https://github.com/Oden-EAG/hp3d.

DEMKOWICZ et al. [26] is outlined in Section 3.2 and in Section 3.3 the method due to Ainsworth and Oden [18] is presented. In Section 3.4 the two variants of self-equilibration algorithms, [19] (Section 3.4.1) and [29] (Section 3.4.2) are detailed.

The error estimation procedures outlined are employed in numerical examples with regular meshes in Section 4. The generalisation for constrained meshes is considered in Section 5. Results to solutions of numerical examples with 1-irregular meshes are presented in Section 6. The application of the error estimation procedures to anisotropic finite elasticity is given in Section 7. Corresponding numerical results for example problems in anisotropic finite elasticity are presented in Section 7.2. We finalize the contribution by a short summary with conclusions (Section 8).

2. Finite Element Method for nearly incompressible materials

We use the standard Lagrangian description of finite elasticity

$$(2.1) x = x(X, t),$$

where X denotes location of a particle at time t = 0 and x a current location at time t. We also introduce the deformation gradient and the right Cauchy–Green tensor and the volume ratio:

(2.2)
$$F = \frac{\partial x}{\partial \mathbf{Y}}, \quad C = F^T F, \quad J = \det(C)^{1/2} = \det(F) > 0.$$

Following Flory [30] we introduce multiplicative decomposition of deformation gradient

(2.3)
$$\bar{F} = J^{-1/3}F, \quad \bar{C} = J^{-2/3}C.$$

With the right Cauchy–Green deformation tensor we associate its invariants:

(2.4)
$$I_1 = \operatorname{tr}(\mathbf{C}), \quad I_2 = \frac{1}{2}[(\operatorname{tr}(\mathbf{C})^2 - \operatorname{tr}(\mathbf{C}^2)], \quad I_3 = \det \mathbf{C},$$

and modified invariants:

(2.5)
$$\bar{I}_1 = \operatorname{tr}(\bar{C}), \quad \bar{I}_2 = \frac{1}{2}[(\operatorname{tr}(\bar{C})^2 - \operatorname{tr}(\bar{C}^2))], \quad \bar{I}_3 = \det \bar{C} = 1.$$

We express the strain energy in terms of invariants:

(2.6)
$$\Psi = \underbrace{\frac{\kappa}{2}(J-1)^2}_{\Psi_{vol}} + \underbrace{\frac{\mu}{2}(\bar{I}_1 - 3) + \frac{c}{2}(\bar{I}_2 - 3)}_{\Psi_{iso}}.$$

The parameters κ , μ and c are empirically determined material constants, κ is called a bulk modulus while μ is a shear modulus. It is known that when $\kappa \gg \mu, c$ then material is nearly incompressible. From the expression for the strain energy we obtain the following constitutive relations for the second Piola–Kirchhoff stress tensor S and the pressure p:

(2.7)
$$\begin{cases} \boldsymbol{S} = -pJ\boldsymbol{C}^{-1} + J^{-2/3}\operatorname{Dev}[\bar{\boldsymbol{S}}], \\ p = -\Psi'_{vol}(J), \\ \bar{\boldsymbol{S}} = 2\frac{\partial\Psi_{iso}}{\partial\bar{\boldsymbol{C}}}, \end{cases}$$

where $\text{Dev}[\bullet] = (\bullet) - \frac{1}{3}[(\bullet) : C]C^{-1}$ is the deviatoric operator.

The boundary-value problem for finite elasticity can be formulated with the first Piola–Kirchhoff stress tensor P = FS as follows: find $\{u, p\}$ such that

(2.8)
$$\begin{cases} -\text{Div } \boldsymbol{P} = \hat{\boldsymbol{b}} & \text{in } \Omega, \\ \boldsymbol{u} = \hat{\boldsymbol{u}} & \text{on } \Gamma_D, \\ \boldsymbol{P} \boldsymbol{N} = \hat{\boldsymbol{t}} & \text{on } \Gamma_N, \end{cases}$$

where \boldsymbol{u} is the displacement, $\boldsymbol{u}=\boldsymbol{x}-\boldsymbol{X}$, and where Ω is the domain occupied by the solid body in the reference configuration. Further, $\hat{\boldsymbol{u}}$ is a prescribed displacement on the Dirichlet boundary Γ_D , and $\hat{\boldsymbol{t}}$ is the load on the Neumann boundary Γ_N , $\hat{\boldsymbol{b}}$ denotes the body forces per unit volume. \boldsymbol{N} is the unit outward normal on Γ_N . Parts of the boundaries Γ_D and Γ_N satisfy the conditions: $\Gamma_D \cup \Gamma_N = \partial \Omega$ and $\Gamma_D \cap \Gamma_N = \emptyset$.

The variational formulation of (2.8) is obtained by multiplication of (2.8₁) by a vector smooth function \boldsymbol{v} , integration over Ω , and integration by parts, and it reads:

(2.9)
$$\int_{\Omega} \mathbf{P} : \nabla \mathbf{v} \, dV = \int_{\Omega} \hat{\mathbf{b}} \cdot \mathbf{v} \, dV + \int_{\Gamma_N} \hat{\mathbf{t}} \cdot \mathbf{v} \, dS.$$

Of course the first Piola–Kirchhoff stress tensor formulation can be replaced by the symmetric second Piola–Kirchhoff stress tensor P = FS, which allows one to involve the symmetric part of the gradient of test functions. Also, when the material is nearly incompressible the finite element formulation can suffer from instability, oscillations and locking. The remedy for this is a 2-field mixed formulation which besides the equilibrium also enforces weakly the constitutive equation for the pressure (2.7_2) . With these two remarks in mind we can write the variational formulation as follows:

$$(2.10) \quad \begin{cases} \int\limits_{\Omega} \frac{1}{2} (\boldsymbol{F}^T \boldsymbol{\nabla} \boldsymbol{v} + \boldsymbol{\nabla}^T \boldsymbol{v} \, \boldsymbol{F}) : \boldsymbol{S} \, dV = \int\limits_{\Omega} \hat{\boldsymbol{b}} \cdot \boldsymbol{v} \, dV + \int\limits_{\Gamma_N} \hat{\boldsymbol{t}} \cdot \boldsymbol{v} \, dS, \quad \forall \boldsymbol{v} \in V, \\ \int\limits_{\Omega} (p + \Psi'_{vol}(J)) q \, dV = 0, \quad \forall q \in Q, \end{cases}$$

where $F = \partial u/\partial X + I$ and S depend on the displacement u and on the pressure, see (2.7) (I stands for the identity matrix). The functional spaces for displacements and for pressure are as follows:

(2.11)
$$V = \{ \boldsymbol{v} \in \{H^1(\Omega)\}^3 : \boldsymbol{v} = 0 \text{ on } \Gamma_D \},$$
$$Q = L^2(\Omega).$$

As far as discretization is concerned, the finite element spaces for the master hexahedron $\hat{K} = [0, 1]^3$ were proposed by Simo, Pister and Taylor [31]:

$$\begin{cases} \hat{Q}^p = \operatorname{span}\{\xi^i \cdot \eta^j \cdot \zeta^k : i, j, k \le p, \, \xi, \eta, \zeta \in [0, 1]\}, \\ \hat{P}^{p-1} = \operatorname{span}\{\xi^i \cdot \eta^j \cdot \zeta^k : i + j + k \le p - 1, \, \xi, \eta, \zeta \in [0, 1]\}. \end{cases}$$

We follow the standard approach. The computational domain Ω is covered with elements K which are images of a master hexahedron \hat{K} in a parametric transformation $T_K \in {\{\hat{Q}^p\}^3 \text{ (i.e., } T_K \text{ is a linear combination of shape functions on } \hat{K})}$ which is invertible:

$$(2.13) K = T_K(\hat{K}).$$

The element faces match for neighboring elements. Then we define the shape functions on the actual elements K:

(2.14)
$$Q^{p}(K) = \{\hat{\psi}(T_{K}^{-1}(\boldsymbol{x})) : \hat{\psi} \in \hat{Q}^{p}\},$$
$$P^{p-1}(K) = \{\hat{\psi}(T_{K}^{-1}(\boldsymbol{x})) : \hat{\psi} \in \hat{P}^{p-1}\}.$$

Finally, the discrete spaces for the whole domain Ω are defined:

(2.15)
$$V_h = \{ \boldsymbol{v} \in \{H^1(\Omega)\}^3 : \boldsymbol{v}_{|K} \in \{Q^p(K)\}^3 \},$$
$$Q_h = \{ q \in L^2(\Omega) : \boldsymbol{q}_{|K} \in P^{p-1}(K) \}.$$

Functions of V_h are continuous while those of Q_h discontinuous on interelement boundaries. Boundary conditions imposed on V_h are analogous as on V.

We anticipate h-adaptivity of the mesh, i.e., a possible subdividing of elements whose estimated error exceeds a prescribed percentage of the maximum element error (strategy of equidistribution of errors of Babuška and Rheinboldt [32]). In the adaptive process we restrict the adaptive meshes to so-called

1-irregular meshes. It means that the ratio of sizes of any neighboring elements does not exceed 1: 2. Continuity of approximation for such meshes is enforced applying multipoint constraints and requires that the special relation of the degrees-of-freedom of the smaller element to the degrees-of-freedom of its larger neighbors is satisfied. Such relations were presented in [33]. We discuss it briefly in Appendix B.

3. Residual implicit error estimates

In this section we consider the error estimation for nonlinear elasticity. The procedure utilizes the approaches applicable for linear problems. The nonlinear procedure is discussed first. Then we outline two error estimation techniques for the linear case, both of implicit type. The first is the element residual method developed by Demkowicz et al. [26] and, in parallel, by Bank and Weiser [34], and the second method is the technique with self-equilibrated residuals designed by Ainsworth and Oden [18]. The last method is used with the two equilibration procedures proposed by Ladevéze and Maunder [19] and Ainsworth and Oden [27].

3.1. The idea to estimate the error due to Rüter and Stein

RÜTER and STEIN in [24] proposed to apply the Helmholtz decomposition of the error expressed by the 1st Piola–Kirchhoff tensor $P - P_h = \nabla \psi + \nabla \times \phi$, with $\psi \in V$ and $\phi \in \{v \in [H^1(\Omega)]^{3\times 3} : (\nabla \times v)N_{|\Gamma_N} = 0\}$. The tensor P_h results from the discrete solution, $P_h = F(u_h)S(u_h, p_h)$. This allows one to represent the residual as follows:

(3.1)
$$R(\boldsymbol{v}) = \int_{\Omega} \hat{\boldsymbol{b}} \cdot \boldsymbol{v} \, dV + \int_{\Gamma_N} \hat{\boldsymbol{t}} \cdot \boldsymbol{v} \, dS - \int_{\Omega} \boldsymbol{P}_h : \nabla \boldsymbol{v} \, dV$$
$$= \int_{\Omega} (\boldsymbol{P} - \boldsymbol{P}_h) : \nabla \boldsymbol{v} \, dV = \int_{\Omega} \nabla \psi : \nabla \boldsymbol{v} \, dV, \quad \forall \boldsymbol{v} \in V.$$

So, we end up with the following equation to evaluate the error function: find $\psi \in V$:

(3.2)
$$(\boldsymbol{\psi}, \boldsymbol{v})_{1,\Omega} = R(\boldsymbol{v}), \quad \forall \boldsymbol{v} \in V.$$

Of course solving exactly this problem in the whole Ω is impossible as it is infinite dimensional and even such a solution for adequately enriched FE space is prohibitively expensive. Therefore it is proposed to estimate $|\psi|_{1,\Omega}$ with a certain error estimation technique. Then the total error of the mixed variational formulation is expressed as in [24]:

$$(3.3) |\boldsymbol{u} - \boldsymbol{u}_h|_{1,\Omega} + \|p - p_h\|_{0,\Omega} \le C(|\boldsymbol{\psi}|_{1,\Omega} + \|\boldsymbol{\Psi}'_{vol} + p_h\|_{0,\Omega}),$$

where C > 0 is a constant depending on the problem. The contribution of the pressure on the right-hand side of (3.3) does not cause any problems: it boils down to computing the L^2 -norm of p_h and $\Psi'_{vol}(J_h)$ with $J_h = \det \mathbf{F}(\mathbf{u}_h)$, resulting directly from the FE analysis. In the following discussion, since components of the error function ψ are decoupled in (3.2), we consider the error estimation techniques limited to the scalar Poisson equation and its weak formulation:

$$(3.4) \begin{cases} -\nabla \cdot (a\nabla u) = f & \text{in } \Omega, \\ u = 0 & \text{on } \Gamma_D, \\ a\frac{\partial u}{\partial n} = \hat{g} & \text{on } \Gamma_N, \end{cases} \iff \begin{cases} B(u,v) = L(v) & \forall v \in V, \\ B(u,v) = \int_{\Omega} a\nabla u \cdot \nabla v \, dV, \\ L(v) = \int_{\Omega} fv \, dV + \int_{\Gamma_N} \hat{g}v \, dS, \end{cases}$$

with a=1. We note that estimation of $|\psi|_{1,\Omega}$ is possible by using the methods typical for linear problems. However, the final estimate of $|u-u_h|$ introduces the constant C which takes into account the analysis of the nonlinear problem, see Brink and Stein [23].

3.2. The implicit error estimate of Demkowicz et al. [26]

The method is quite inexpensive and it leads to satisfactory results. The basic step of the method is to define an enriched space of element shape functions $V_{h,p+1}(K) = \{Q^{p+1}(K)\}^3$, with polynomial order p+1. In this space we define the kernel of the interpolation operator Π_{hp}^3 :

(3.5)
$$M_K = \{ v \in V_{h,p+1}(K) : \Pi_{hp}v = 0 \}.$$

In other words M_K consists of element shape functions of p+1 order which vanish at the interpolation points (for instance of the Lagrangian type). Next, we consider the element residual of the form:

(3.6)
$$r_K(v) = \int_K (f + \nabla \cdot (a\nabla u_h))v \, dx + \int_{\partial K \cap \Gamma_N} \left(\hat{g} - a\frac{\partial u_h}{\partial n}\right) \cdot v \, dS + \int_{\partial K \setminus \partial \Omega} \frac{1}{2} \left[\left| a\frac{\partial u_h}{\partial n} \right| \right] \cdot v \, dS,$$

³First, we define interpolation on the master element: $(\hat{\Pi}_{hp}\hat{\boldsymbol{v}})(\boldsymbol{\xi}) = \sum_{i=1}^{(p+1)^3} \hat{\boldsymbol{v}}(\boldsymbol{\xi}_i)\hat{l}_i(\boldsymbol{\xi})$, where $\hat{\boldsymbol{v}}(\boldsymbol{\xi}) = \boldsymbol{v}(T_K(\boldsymbol{\xi}))$ and $\boldsymbol{\xi}_i, \hat{l}_i, i = 1, \dots, (p+1)^3$ are the Lagrangian points and polynomials on $\hat{K} = [0, 1]^3$. Then $(\Pi_{hp}\boldsymbol{v})(\boldsymbol{x}) = (\hat{\Pi}_{hp}\hat{\boldsymbol{v}})(T_K^{-1}(\boldsymbol{x}))$.

where $[|a \partial u_h/\partial n|]$ denotes the jump of the flux between the neighboring element and element K. We formulate the local boundary-value problem in the kernel M_K : find $\phi_K(\mathbf{x}) \in M_K$ such that:

(3.7)
$$B_K(\phi_K, v) = r_K(v), \quad \forall v \in M_K,$$

where B_K is a restriction of the form $B(\cdot, \cdot)$ to the element K. The error estimate in the energy norm $\|\cdot\|_E = B(\cdot, \cdot)^{1/2}$ can be found as:

(3.8)
$$||u_h - u||_E^2 \le C \sum_K ||\phi_K||_{E,K}^2,$$

where summation goes through all elements in the mesh, and where C is a parameter growing moderately with p. We note that the residual can be expressed in an alternative way (after integrating by parts the second derivatives of the first integral):

(3.9)
$$r_K(v) = B_K(u_h, v) - L_K(v) + \int_{\partial K \setminus \partial \Omega} \left\langle a \frac{\partial u_h}{\partial n} \right\rangle v \, dS,$$

where $\langle a \partial u_h/\partial n \rangle$ denotes the average flux between the elements. This form is similar to the method of equilibrated residuals discussed below.

3.3. Residual error estimate with self-equilibration of residuals

The technique with self-equilibration of residuals caused a sort of revolution in the area of error estimation. It was proposed by Ainsworth and Oden [18]. This method results in estimates without any scaling constants thus displaying the direct error in the energy norm. The self-equilibration plays the essential role as one can solve the purely Neumann local residual problems on elements.

We represent the global residual functional as the following sum of element contributions:

(3.10)
$$r(u_h, v) = B(u_h, v) - L(v) = \sum_K (B_K(u_h, v) - L_K(v))$$

$$= \sum_K \underbrace{(B_K(u_h, v) - L_K(v) - \lambda_K(v))}_{r_K(v)}$$

$$= \sum_K r_K(v), \quad \text{with } \sum_K \lambda_K(v) = 0,$$

(all summations go through all elements of the mesh). Above $\lambda_K(v)$ there are linear functionals constructed for elements K, and the last condition is required

to keep consistency of the global residual $\Sigma_K(B_K(u_h,v)-L_K(v))$ with the residual augmented by λ_K , i.e., $\Sigma_K(B_K(u_h,v)-L_K(v)-\lambda_K(v))$. B_K and L_K are restrictions of forms B and L to the element K, respectively. In addition, we construct the functionals λ_K in such a way that:

(3.11)
$$r_K(1) = 0$$
, for all elements K .

This condition implies the self-equilibration of the residuals as a constant function in the null space of the Poisson equation. Self-equilibration allows one to solve the local purely Neumann problems on the elements of the form: find $\phi_K \in V(K) = H^1(K)$ such that:

(3.12)
$$B_K(\phi_K, v) = r_K(v), \quad \forall v \in V(K).$$

This results in the following estimate:

(3.13)
$$||u_h - u||_E^2 \le \sum_K ||\phi_K||_{E,K}^2.$$

Note that there is no auxiliary constant scaling the estimate. As the problem (3.12) is infinite dimensional, one solves it in the enriched polynomial space of shape functions of the element. Usually these are p+1 order polynomials.

3.4. Self-equilibration of residuals

The essential problem of the Ainsworth and Oden error estimation technique is self-equilibration of residuals understood as in Eq. (3.11), i.e., that element residuals vanish for constant test functions. The most important issue is whether one can solve this problem locally, without involving all the elements in the mesh. Such an algorithm actually exists. We elaborate the algorithm of Ladevéze and Maunder [19, 20] and the one proposed by Ainsworth and Oden [18, 27].

3.4.1. Algorithm of Ladevéze and Maunder. We define the average flux between elements K and L over their common face:

(3.14)
$$\bar{t}_K = \frac{1}{2} ((a \nabla u_h)^K + (a \nabla u_h)^L) \cdot \boldsymbol{n}_K,$$

where n_K is a unit normal vector on the surface of the element K. Next, we wish to find a function $\theta_K(s): R^3 \ni s \to \theta_K \in R$, where s is a location on the boundary ∂K , to satisfy the following conditions for all 8 trilinear functions ψ_K^n associated with vertices of the element K:

(3.15)
$$r_K = B_K(u_h, \psi_K^n) - L_K(\psi_K^n) - \int_{\partial K} \bar{t}_K \psi_K^n dS - \int_{\partial K} \theta_K \psi_K^n dS = 0,$$

$$n = 1, \dots, 8.$$

Here G_K^n is a known part of the element residual while $\theta_K(s)$ is to be found. Ladevéze called these statements prolongation conditions. We note that, since $\Sigma_{n=1}^8 \psi_K^n = 1$, summation of (3.15) implies equilibrium as in (3.11). We postulate that the function $\theta_K(s)$ is a linear combination of 4 bilinear functions on each face f of element K:

(3.16)
$$\theta_{K|f}(s) = \sum_{n=1}^{4} \theta_n^f \cdot \psi_{K|f}^n(s),$$

where θ_n^f are the coefficients to be found. Using the known parameters G_K^n as noted in (3.15), we can write the prolongation conditions in the form:

(3.17)
$$\int_{\partial K} \theta_K(s) \psi_K^n(s) dS = G_K^n, \quad n = 1, \dots, 8.$$

In this way we reduced the problem of finding $\theta_K(s)$ to obtain for each element K, 4×6 parameters θ_n^f , such that functions $\theta_{K|f}(s)$ are identical but opposite for the neighboring elements. It turns out that a solution of this problem is possible by considering vertex nodes of the element K separately. The typical situation of a regular mesh is shown in Fig. 1.

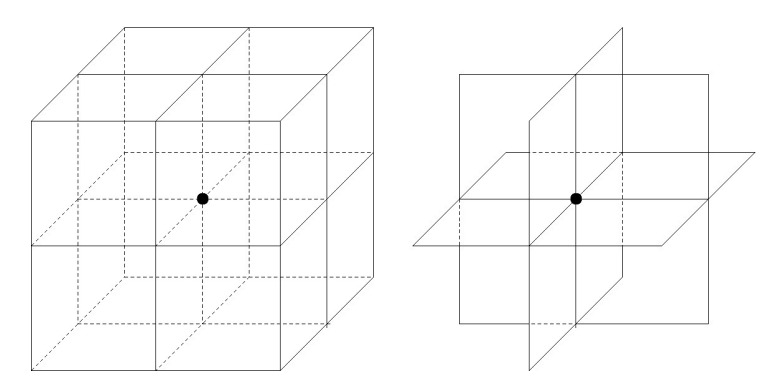


Fig. 1. Typical situation: 8 hexes surrounding one vertex and the corresponding 12 faces adjacent to this vertex.

This solution can be obtained as follows.

For a fixed vertex n of the element K, let the unknown contributions to the integral on the left-hand side of (3.17) be denoted as $g_K^{n,f}$:

(3.18)
$$\int_{\partial K} \theta_K \psi_K^n dS = \sum_{f \in \text{supp}(\psi_K^n)} g_K^{n,f}, \text{ where } g_K^{n,f} = \int_f \theta_K \psi_K^n dS.$$

With this notation the prolongation conditions take the form:

(3.19)
$$\sum_{f \in \text{supp}(\psi^n)} g_K^{n,f} = G_K^n, \quad n = 1, \dots, 8.$$

We assume that vertex n belongs to N neighboring elements of K (N=8 in the example of Fig. 1). Each element has 3 faces adjacent to vertex n, and each face is common to 2 elements. This means that we have 3/2N independent parameters d_i corresponding to unknown coefficients θ_n^f (we have $3/2 \cdot 8 = 12$ in the example). Let's denote by i(K, f) appropriate indices of d_i , and by $\operatorname{sgn}(K, f) = \pm 1$ the corresponding signs connecting d_i and $g_K^{n,f}$:

(3.20)
$$g_K^{n,f} = d_{i(K,f)} \cdot \operatorname{sgn}(K,f), \quad \forall K \in \operatorname{supp}(\psi^n).$$

With this notation we state the prolongation conditions as follows:

(3.21)
$$\sum_{f \in \operatorname{supp}(\psi^n) \cap \partial K} d_{i(K,f)} \cdot \operatorname{sgn}(K,f) = G_K^n, \quad \forall K \in \operatorname{supp}(\psi^n),$$

or in the matrix form:

$$(3.22) Ad = G.$$

The above system of N equations with 3/2N unknowns is underdetermined. Its explicit form is shown in Fig. 2 (for an example rectangular mesh). We can solve it by considering the minimization of function $d^T M d$, with M being a selected

$$\underbrace{\begin{bmatrix} +1 & +1 & +1 & +1 & \\ -1+1 & & +1 & \\ -1+1 & & +1 & \\ & -1+1 & & +1 & \\ & & +1 & & -1 & \\ & & +1 & & -1 & \\ & & & -1+1 & +1 & -1 \\ & & & & -1-1 & & -1 \end{bmatrix}}_{A} \underbrace{\begin{bmatrix} d_1 \\ d_2 \\ \vdots \\ \vdots \\ \vdots \\ \vdots \\ d_{12} \end{bmatrix}}_{C} = \underbrace{\begin{bmatrix} G_1 \\ G_2 \\ \vdots \\ \vdots \\ \vdots \\ G_8 \end{bmatrix}}_{C}$$

Fig. 2. Explicit form of system of equation (3.22) (the empty entries correspond to zero).

symmetric positive definite matrix and under the condition that Ad = G, using the method of Lagrange multipliers $\Lambda \in \mathbb{R}^N$:

(3.23)
$$\begin{cases} \frac{1}{2} d^T M d = \min, \\ A d = G, \end{cases} \Longrightarrow \begin{cases} M d + A^T \Lambda = 0, \\ A d = G. \end{cases}$$

Having found the parameters d_i for all faces attached to the subsequent corners n, we can go back to find the parameters θ_n^f . We use the definition of $g_K^{n,f}$ (3.18) and the postulated expansion of function $\theta_{K|f}$ (3.16):

(3.24)
$$g_K^{n,f} = \int_f \underbrace{\left(\sum_{m=1}^4 \theta_m^f \psi_{K|f}^m\right)}_{\theta_{K|f}} \psi_{K|f}^n dS, \quad n = 1, \dots, 4 \rightarrow g_K^{nf} = \sum_{i=1}^4 \mu_{mn} \theta_m^f,$$

where $\mu_{mn} = \int_f \psi^m_{K|f} \psi^n_{K|f} dS$, is the mass-like matrix. Selection of the matrix M could reflect the geometry of elements surrounding the vertex n. However, for meshes close to uniform we selected M = dia(1, ..., 1).

3.4.2. Algorithm of Ainsworth and Oden. In this method we consider a similar condition as in Ladevéze:

$$(3.25) \underbrace{B_K(u_h, \psi_K^n) - L_K(\psi_K^n) - \int_{\partial K \setminus \partial \Omega} \bar{t}_K \psi_K^n \, dS - \int_{\partial K \setminus \partial \Omega} \psi_K^n(s) \cdot \mu_{KL}(s) \left[\left| a \frac{\partial u_h}{\partial n} \right| \right] dS = 0,}_{G_K^n}$$

where functions $\mu_{KL}(s)$, are to be found between elements K and L, with a condition that $\mu_{KL} = -\mu_{LK}$ (to satisfy the requirement that $\Sigma_K \lambda_K = 0$). The procedure to evaluate functions $\mu_{KL}(s)$ is as follows:

First we define the quantity for a face between elements K and L:

(3.26)
$$\rho_{KL}^{n} := \int_{\Gamma_{KL}} \psi_{K}^{n}(s) \left[\left| a \frac{\partial u_{h}}{\partial n} \right| \right] dS,$$

which can be called "jumps of the fluxes". Next, we solve for coefficients μ_{KL}^n for the element K and all its neighbors L:

(3.27)
$$\sum_{L} \underbrace{\mu_{KL}^{n} \rho_{KL}^{n}}_{\hat{\mu}_{KL}} = G_{K}^{n} \rightarrow \sum_{L} \hat{\mu}_{KL}^{n} = G_{K}^{n} \rightarrow \hat{\mu}_{KL}^{n} \rightarrow \mu_{KL}^{n} = \frac{\hat{\mu}_{KL}^{n}}{\rho_{KL}^{n}}.$$

The summation in (3.27) runs over all neighbors L of the element K. The system of equations, the second version in (3.27), is identical as the system (3.22) previously considered in the Ladevéze and Maunder method, so we can solve it in identical manner. Finally, the functions $\mu_{KL}(s)$ are expressed by the above found coefficients μ_{KL}^n by interpolating them using vertex trilinear shape functions:

(3.28)
$$\mu_{KL}(s) = \sum_{n=1}^{8} \psi_K^n(s) \mu_{KL}^n.$$

It can be verified that $\mu_{KL}(s)$ satisfy the condition (3.25) with ψ_K^n being replaced by a unit function 1:

(3.29)
$$r_k(1) = G_K^n(1) - \int_{\partial K \setminus \partial \Omega} 1 \cdot \mu_{KL}(s) \left[\left| a \frac{\partial u_h}{\partial n} \right| \right] dS = 0,$$

which means equilibrium of the residual r_K .

In the procedure outlined above there is a problem of zeroing of the flux jump defined in Eq. (3.26) that appears in denominator of computing μ_{KL}^n (3.27). This issue was addressed in [27]. The face suffering from this is simply excluded from the minimization process of solving an underdetermined system. Actually, this could be also done if value of μ_{KL}^n exceeds a prescribed limit.

3.5. Final remarks on error estimation

The method with self-equilibration of residuals [18] is more expensive then the procedure of DEMKOWICZ et al. [26]. The computational cost of the method of AINSWORTH and ODEN is estimated in [27]. The cost of self-equilibration is actually proportional to the number of vertex nodes in the mesh N_v and it boils down to solving the systems of equations of dimension n_f , a number of walls meeting at vertices, compare Eq. (3.23). This cost is $1/3N_vn_f^3$ (for a regular hexahedral mesh we have $n_f = 12$). The remaining cost of self-equilibration can be comparable as in computation of the Demkowicz et al. method – computing flux jumps. However, the major difference is in the dimension of the residual equations being solved, i.e., Eqs. (3.7) and (3.12). The first is of the dimension of M_K : $(p+1)^3 - p^3 = 3p^2 + 3p + 1$ while the second: $(p+2)^3$ (the dimension of the enriched element space). Thus we have the order of p difference. Having said this, we remark that both procedures can be processed in parallel which makes them very inexpensive.

The ratio of the estimated global error and the actual error $|\boldsymbol{u} - \boldsymbol{u}_h|_{1,\Omega}$, known as an effectivity index, is found in the following numerical tests using for comparison the solutions on meshes of the order p=3. These effectivity indices and global error indicators were listed in Appendix A.

4. Numerical examples for regular meshes

In this section we start presenting numerical tests illustrating the practical performance of the error estimation techniques. We select typical examples: pressurization of a tube and bending of a body with re-entrant corners. First we show the performance on regular finite element grids. In our interest is exclusively the displacement part of the error, as the pressure contribution requires much less effort (explicitly: p_h and $\Psi'_{vol}(J_h)$ in (3.3), with $J_h = \det \mathbf{F}(\mathbf{u}_h)$, result from the FE analysis [23, 24]).

We are interested in comparing the quality of the error estimation methods. As a measure of their compatibility we evaluate the correlation coefficients for the subsequent pairs of techniques. We consider this investigation informally as it rather characterizes statistical phenomena, not determined problems. The tables of the correlation coefficients are posted in Appendix A.

Pressurisation of a tube

We consider a tube of the internal radius $r_{\rm in}=3.13$, thickness t=0.744 and height h=10. It occupies 90° in the circumferential direction. The tube is made of elastic material with $\kappa=100\,000$, $\mu=2.536\cdot 10^{-3}$ and c=0. It is clamped at the bottom and we impose no-penetration condition at the top and side boundaries. It is loaded with an internal pressure $p=0.4\cdot 10^{-3}$. Figures 3 a–c show the displacements u_z and u_r and distribution of the effective stress σ_0 on the sur-

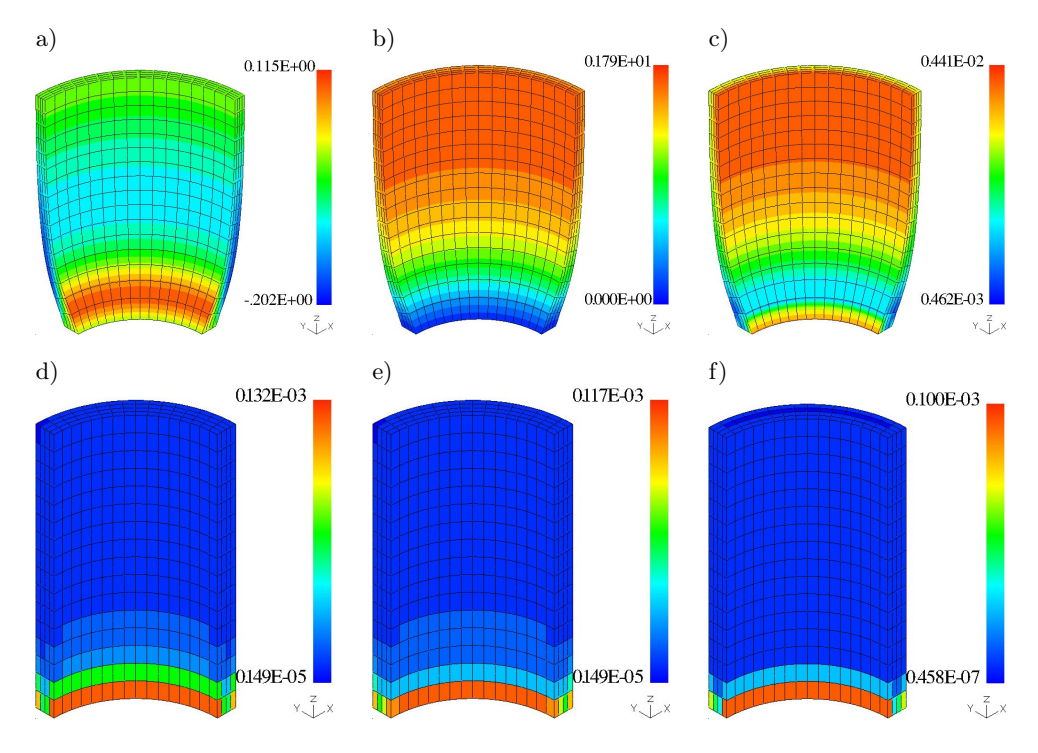


Fig. 3. Pressurization of a tube. Solution: a) u_z , b) u_r , c) σ_0 . Errors: d) Ainsworth/Oden, e) Ladevéze/Maunder, f) Demkowicz *et al.*

face of deformed configuration. In Figs. 3 d–f we present the distribution of error indicators obtained with the self-equilibration technique with Ainsworth/Oden, Ladevéze/Maunder methods and the Demkowicz *et al.* procedure.

Bending of "tire tread"

In our next example we consider the specimen whose vertical cross-section forms a T-shape domain. Such a shape is typical for testing adaptivity as it displays high stress concentration in the re-entrant corners (for linear elasticity one observes singularity at these corners). For convenience we call it "tire tread". Its base is a cuboid of horizontal dimensions L=6.0 and D=3.0, and height h=1.0. The upper part, in the yz-plane cross-section is a square of dimension a=1.0. In the xy-plane it forms two cylinders of radii $r_{\rm in}=2.5, r_{\rm ex}=3.5$, and concave in the negative and positive y-directions. The "tire tread" is clamped on the bottom of its base and the remaining boundary is free. The material data are as in the previous example. We put the load of $\hat{t}_y=0.3\cdot 10^{-3}$ on the upper-most surface.

Figure 4a shows the displacement u_y on the deformed configuration. The remaining Figs. 4b–d present the distribution of error estimates.

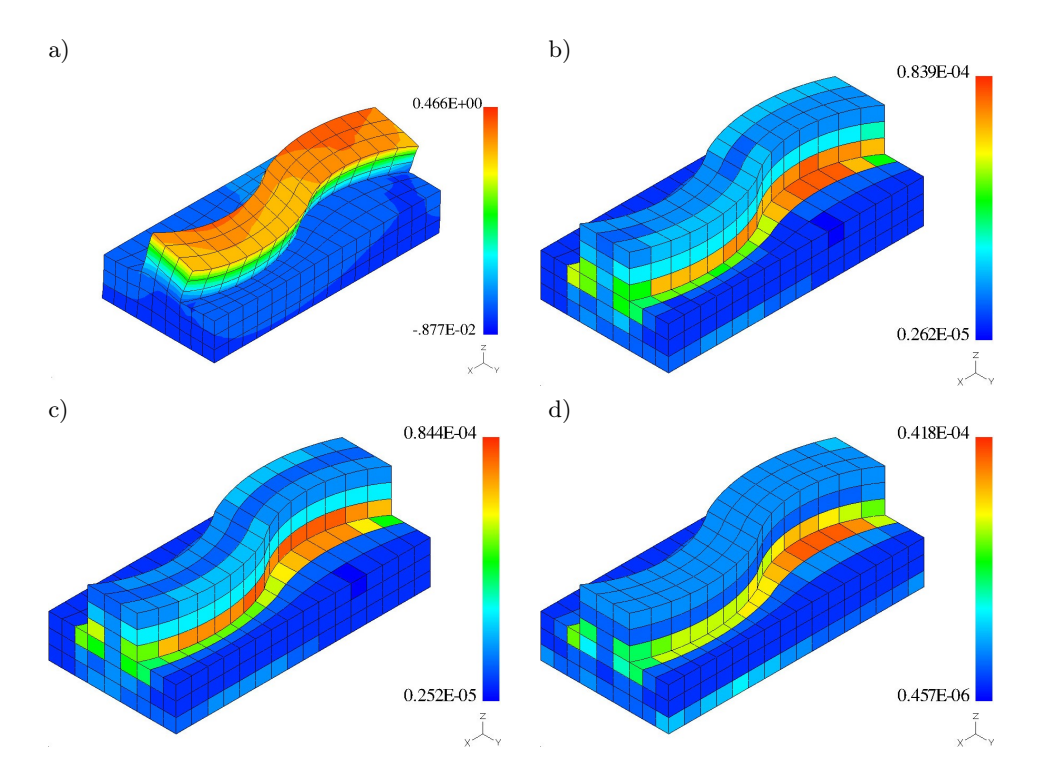


Fig. 4. "Tire tread". a) solution u_y (on deformed configuration). Errors: b) Ainsworth/Oden, c) Ladevéze/Maunder, d) Demkowicz $et\ al.$

Pressurisation of an irregular tube

In our third example we consider a cylindrical tube with three bumps which make their geometry irregular. The inner radius of the tube $r_{\rm in}=0.5756$, the thickness t=0.2718 and height h=2.1. The tube occupies the angle of 90° in the circumferential direction. The tube is subject to no-penetration boundary conditions on bottom, top and side walls. The material data are as before. The loading internal pressure is $p=0.4\cdot10^{-3}$. We delay presentation of characteristics of the solution until we show the solution on an adaptive mesh (see Fig. 11). Here we just present the distribution of the three error estimates which are presented in Fig. 5.

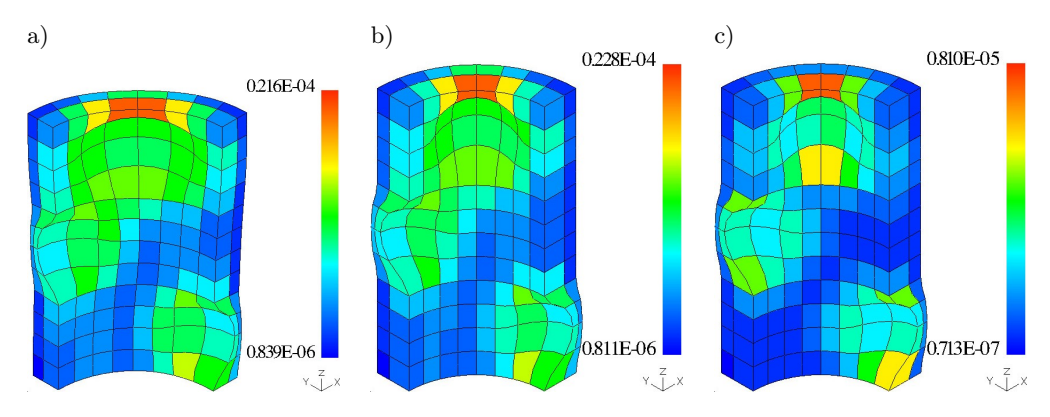


Fig. 5. Irregular tube. Errors: a) Ainsworth/Oden, b) Ladevéze/Maunder, c) Demkowicz *et al.*

5. Generalization for constrained meshes

In this section we discuss generalization of self-equilibration procedures for constrained meshes. The term "constrained" comes from the fact in the adaptation process selected subdivision of elements create the situations where smaller elements are attached to the larger neighbors, with the assumption that the ratio of their sizes does not exceed 1:2 (when we limit ourselves to 1-irregular meshes). In order to satisfy continuity of approximation one has to modify the shape functions and the degrees-of-freedom (dof) of the smaller elements so that they would coincide with those of the larger elements. Such a procedure in the adaptive code is fully automatic and it boils down to the following linear transformation between the standard degrees-of-freedom u_i and shape functions ψ_i and their constrained counterparts U_i and Ψ_i :

(5.1)
$$\Psi_i = \sum_j R_{ij} \psi_j \quad \text{and} \quad u_i = \sum_j U_j R_{ji},$$

where ranges of indices j are adequately limited to the shape functions or dof involved in the constraints. More precise discussion of constrained approximation is presented in Appendix B. Figure 6 shows an example of a smaller element attached to larger neighbors and values of shape function assuming value 1 at the vertex in the back, and vanishing at the remaining 7 constrained vertices (marked in black), i.e., those affecting trilinear approximation in a smaller element. These constrained vertices are located on sides of the larger neighbors, even outside of the strict domain of the smaller element. Can the self-equilibration procedure be applied in such situations?

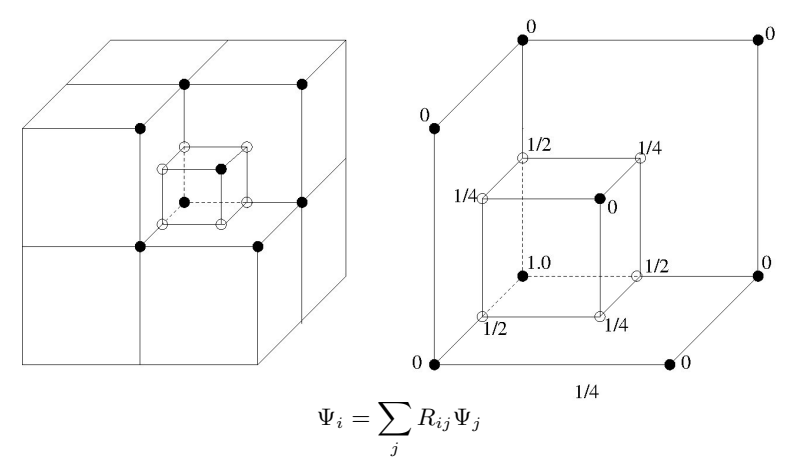


FIG. 6. Illustration of a constrained shape function Ψ_i associated with a central vertex node. Coefficients R_{ij} expressing the constrained shape function Ψ_i by ordinary shape functions ψ_j are found automatically for every element. Actual vertices, i.e., those which contain the unconstrained degrees-of-freedom (dofs), are marked as \bullet , while the hanging (constrained) vertices are marked as \circ . Dofs of hanging vertices are constrained by dofs of actual vertices, see Appendix B.

Equilibration for Ladevéze/Maunder procedure

Let us first discuss the Ladevéze/Maunder algorithm for which the 3D constrained case was considered by RACHOWICZ [20]. Let us take into account all constrained vertices of a smaller element as in Fig. 7, where they are marked as black circles • while the hanging vertices are denoted as \circ . Focusing our attention on one of constrained vertices we first generate a patch of attached elements as a collection of elements where the constrained global shape function associated with this vertex is nonzero. Then we identify all the faces of elements which are internal of the patch (i.e., not on its boundary). For a selected element K we can write the definition of G_K^n using the constrained shape function Ψ_K^n :

(5.2)
$$\int_{\partial K} \theta_K(\mathbf{s}) \Psi_K^n(\mathbf{s}) dS = G_K^n,$$

where

(5.3)
$$G_K^n = B_K(u_h, \Psi_K^n) - L_K(\Psi_K^n) - \int_{\partial K} \bar{t}_K \Psi_K^n dS,$$

i.e., ordinary shape functions ψ_K^n were replaced by constrained Ψ_K^n . We still have the property that $\Sigma_{n=1}^8 \Psi_K^n(x) = 1$ for constrained functions. We also change accordingly the parameter $g_K^{n,f}$:

$$g_K^{n,f} = \int_f \theta_K \Psi_K^n \, dS,$$

and it yields the equation:

(5.5)
$$\sum_{f \in \text{supp}(\Psi^n)} g_K^{n,f} = G_K^n,$$

where we used the support of a constrained global shape function. Obviously, the number of internal faces of elements exceeds the number of elements in the patch. Therefore, one can solve the above prolongation condition as an underdetermined system which results in parameters $g_K^{n,f}$. However, we would have a problem if we try to go back to coefficients θ_m^f : we have 4 parameters for each face, and there can be more than 4 constrained shape functions defining solution on some faces of the smaller element. The example of such a face is shown in Fig. 7a, where the solution depends on 7 constrained vertices. On the other hand, for some faces the solution depends only on 4 vertices, see Fig. 7b. So what can we do?

Simply we can utilize the fact that the number of internal faces of the patch exceeds the number of elements in the patch, and we can *exclude* such faces from

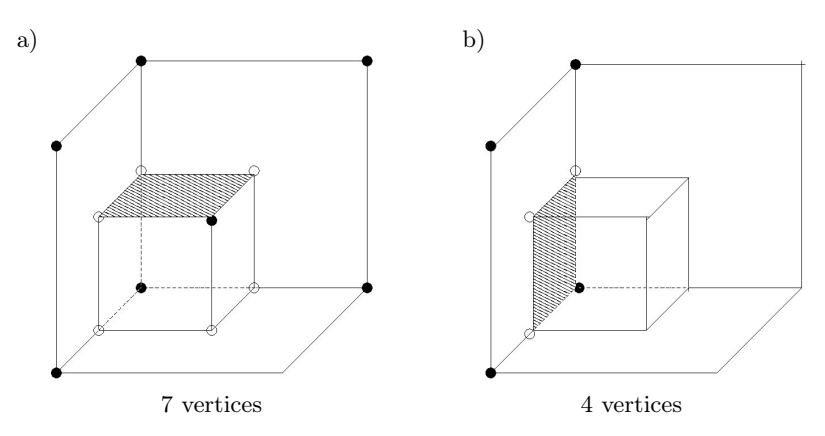


Fig. 7. Constrained faces where value of approximation depends on: a) values in 7 vertices • – should be excluded in the algorithm, b) values in 4 vertices • – should be included in the algorithm, (we mark by ∘ the "hanging" vertices).

solving the underdetermined system: it just boils down to erasing the appropriate column in the system corresponding to that shown in Fig. 2.

The number of faces that are left out still exceeds the number of elements in the patch (if not – it would alarm us – but it never happens). The solution that we propose leaves the flux on such (excluded) faces uncorrected from their initial value: as the average between the elements.

Equilibration for Ainsworth/Oden procedure

As far as the method of Ainsworth/Oden is concerned we notice that the procedure can be formulated with constrained shape functions without any modification. The proof that the resulting element residual is self-equilibrated, shown in paper [18], uses the fact that both, ordinary and constrained shape functions sum up to 1:

(5.6)
$$\sum_{n=1}^{8} \psi_{K}^{n}(\boldsymbol{x}) = 1 \text{ and } \sum_{n=1}^{8} \Psi_{K}^{n}(\boldsymbol{x}) = 1.$$

This means that replacing ordinary shape functions ϕ_K^n for unconstrained meshes by constrained shape functions Ψ_K^n for adaptive meshes results in self-equilibration of element residuals. (This fact perhaps was not explicitly stated in papers [18, 27] but it was expressed by the illustrating figures).

Figure 8 presents a general structure of the algorithm of self-equilibration for both, AINSWORTH and ODEN [18] and LADEVÉZE and MAUNDER [19] procedures.

```
for vert=1,8 ! main loop through vertices
   find elements attached to vert, list(1:nrel)
   for i=1,nrel ! loop through elements in patch to collect faces
       for wall=1,6
           collect and classify faces attached to vert
       endfor wall
   endfor i
   for i=1,nrel ! loop through elements to generate system of equations
       find augmented residual of element G_K^n
       for wall=1,6
           build equation for face A_{i,j}
       endfor wall
   endfor i
   solve system of eq. for d_i (or \mu_{KL})
endfor vert
Develop equilibrated residual r_K
Solve Neumann problem for \phi_K
Evaluate error e_K
```

Fig. 8. An algorithmic representation of the procedure of self-equilibration.

6. Numerical examples for 1-irregular meshes

In this section we present the numerical examples for h-adaptive meshes. In case of the "tire tread" example we applied 2 levels of h-refinements based on the Demkowicz $et\ al.$ error indicators. The refined mesh and the deformation together with displacement u_y are shown in Fig. 9a. The remaining panels b, c and d of this figure present the distribution of the three error indicators. One can see quite significant resemblance of the first two of them and some departure in the Demkowicz $et\ al.$ We also present the rate of convergence for the solutions on adaptive meshes in Fig. 10. We display the H^1 -seminorm of the error obtained by comparing the adaptive solutions with the solutions on the meshes of the order p=3.

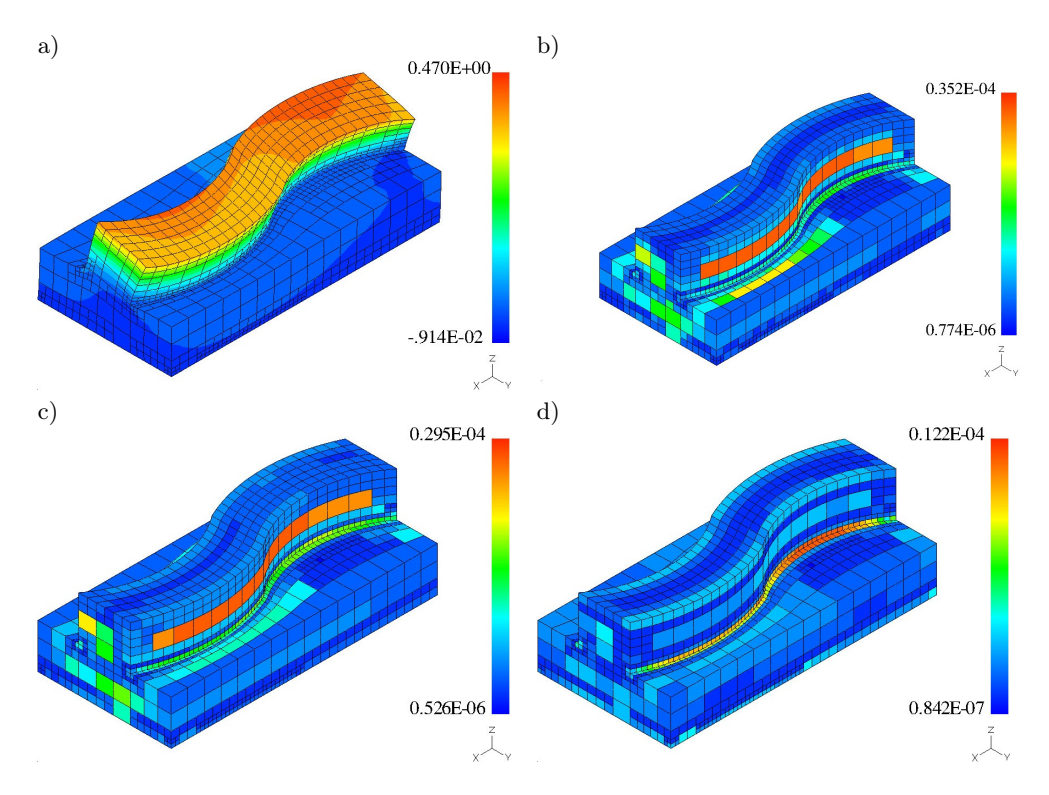


Fig. 9. "Tire tread". a) solution u_y . Errors: b) Ainsworth/Oden, c) Ladevéze/Maunder, d) Demkowicz $et\ al.$

In Fig. 11 we show some characteristics of the solution of the pressurized irregular tube: displacements u_r , u_θ and pressure p, on the deformed configuration. The distributions of error indicators corresponding to three investigated techniques are presented in Fig. 12. We observe a general resemblance

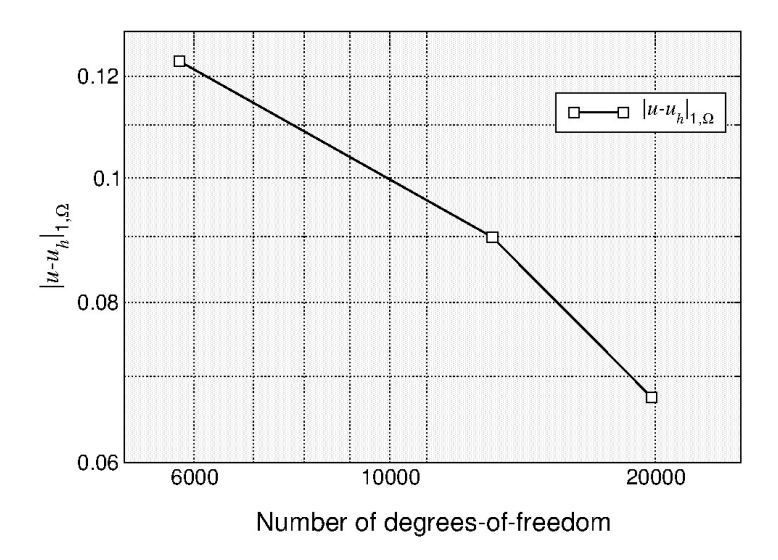


Fig. 10. "Tire thread". Convergence of the H^1 -seminorm error for the h-adaptive meshes.

of these distributions. The range of magnitude of these error indicators is much less then in the "tire tread" problem as there is no such significant stress concentration as in that case. In Fig. 13 the rate of convergence is presented for the solutions on adaptive meshes. The H^1 -seminorm of the error is obtained as before by comparing with adaptive solutions with those obtained on the enriched meshes.

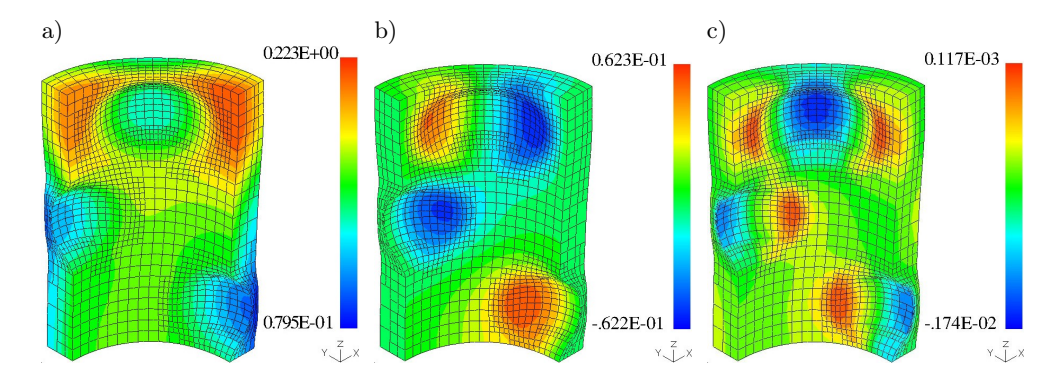


Fig. 11. Irregular tube. Solution components: a) u_r , b) u_θ , c) pressure p (on deformed configuration).

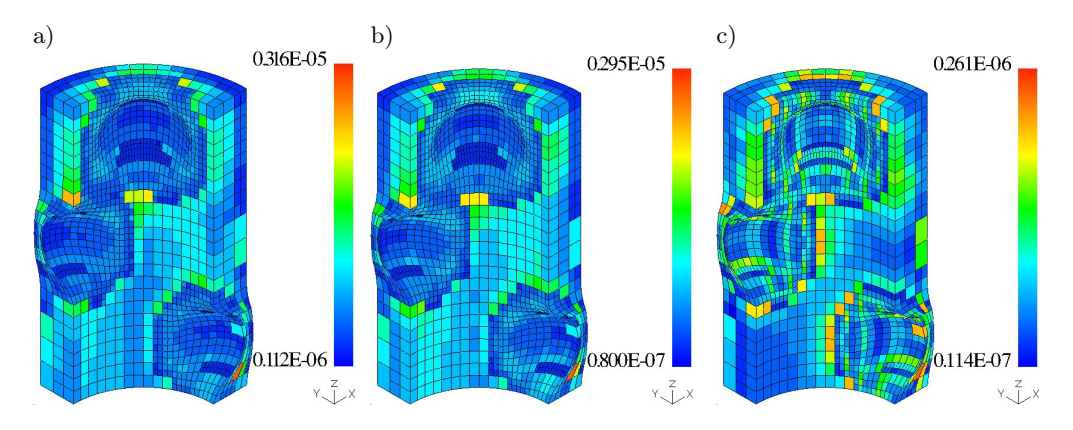


Fig. 12. Irregular tube. Errors: a) Ainsworth/Oden, b) Ladevéze/Maunder, c) Demkowicz *et al.*

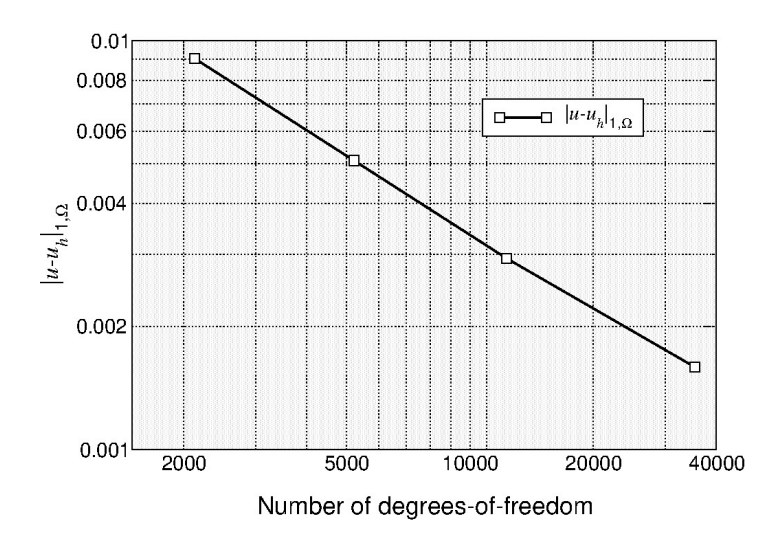


Fig. 13. Irregular tube. Convergence of the H^1 -seminorm error for the h-adaptive meshes.

7. Application for anisotropic elasticity

We can also apply the presented error estimation techniques for more general models such as anisotropic finite elasticity. We discuss here the application to an elasticity model in which the anisotropy results from the reinforcement by two stiff families of fibres. Such a model was presented by ZDUNEK and RACHOWICZ in [8]. We briefly outline this approach. For details we direct the reader to this paper.

7.1. Anisotropic elasticity

The reinforcing families are represented by the two fibre directions:

(7.1)
$$G_F(X), |G_F| = 1, F = 1, 2,$$

sometimes called preferred directions. They define two structural tensors:

(7.2)
$$A_F := G_F \otimes G_F \text{ (no sum)}, \quad F = 1, 2.$$

Apart from the defined before invariants I_1, I_2 and I_3 we now define the joint invariants of C and A_F , namely I_4, \ldots, I_8 :

(7.3)
$$I_4 = \mathbf{C} : \mathbf{A}_1, \ I_5 := \mathbf{C}^2 : \mathbf{A}_1, I_6 = \mathbf{C} : \mathbf{A}_2, \ I_7 := \mathbf{C}^2 : \mathbf{A}_2, \ I_8 := \mathbf{G}_1 \cdot \mathbf{C}\mathbf{G}_2(\mathbf{G}_1 \cdot \mathbf{G}_2).$$

The strain energy can be expressed by the whole set of invariants $\Psi(I_1, \ldots, I_8)$. If contribution to the strain energy corresponding to I_4, \ldots, I_8 dominates the contribution of I_1 , I_2 , I_3 the material is nearly inextensible in the preferred directions. In such a case application of just displacement formulation of the finite element method may cause danger of numerical locking and oscillations analogous as for nearly incompressible materials.

To obtain the resulting constitutive relations it is convenient to express the kinematics in convected coordinates. We define the direction orthogonal to fibres:

$$(7.4) G_3 := G_1 \times G_2/|G_1 \times G_2|.$$

We consider curvilinear co-ordinates $X = X(\xi^A)$ generating the basis:

(7.5)
$$\{G_A\}, A = 1, 2, 3: G_A = \partial X/\partial \xi^A,$$

and its dual $\langle \underline{\mathbf{G}}^A, \mathbf{G}_B \rangle = \delta_B^A$, A, B = 1, 2, 3. Convected spatial coordinates are generated by a parametrization:

(7.6)
$$\mathbf{x} = \mathbf{x}(\zeta^a), \ \zeta = \boldsymbol{\xi}: \ \mathbf{g}_a = \partial \mathbf{x}/\partial \zeta^a, \ \langle \mathbf{g}^a, \mathbf{g}_b \rangle = \delta_b^a, \ (\{\mathbf{g}^a\} - \text{dual basis}).$$

The deformation gradient F, its adjoint F^* and their inverses take the form:

(7.7)
$$\mathbf{F} = \delta_A^a \mathbf{g}_a \otimes \underline{\mathbf{G}}^A, \quad \mathbf{F}^{-1} = \delta_a^A \mathbf{G}_A \otimes \underline{\mathbf{g}}^a,$$
$$\mathbf{F}^* = \delta_A^a \underline{\mathbf{G}}^A \otimes \mathbf{g}_a, \quad \mathbf{F}^{-*} = \delta_a^A \mathbf{g}^a \otimes \mathbf{G}_A.$$

The material and spatial metric tensors $G_{AB} = \mathbf{G}_A \cdot \mathbf{G}_B$ and $g_{ab} = \mathbf{g}_a \cdot \mathbf{g}_b$ are expressed as follows:

(7.8)
$$G = G_{AB}\underline{G}^A \otimes \underline{G}^B \text{ and } g = g_{ab}\underline{g}^a \otimes \underline{g}^b.$$

Finally, the right Cauchy–Green deformation tensor takes the form:

(7.9)
$$C = F^* g F, \quad C = \delta_A^a \delta_B^b g_{ab} \underline{G}^A \otimes \underline{G}^B.$$

In turn, the invariants of C and joint invariants of C and A_F , F = 1, 2, can be written as:

(7.10)
$$I_{1} = \langle \boldsymbol{G}^{-1}\boldsymbol{C}, \boldsymbol{I} \rangle, \ I_{2} = \langle \operatorname{cof}(\boldsymbol{C})\boldsymbol{G}, \boldsymbol{I} \rangle, \ I_{3} = \det(\boldsymbol{G}^{-1}\boldsymbol{C}),$$
$$I_{4} = \langle \boldsymbol{C}, \boldsymbol{A}_{1} \rangle, \quad I_{5} = \langle \boldsymbol{C}^{2}, \boldsymbol{A}_{1} \rangle,$$
$$I_{6} = \langle \boldsymbol{C}, \boldsymbol{A}_{2} \rangle, \quad I_{7} = \langle \boldsymbol{C}^{2}, \boldsymbol{A}_{2} \rangle, \quad I_{8} = \boldsymbol{G}_{1} \cdot \boldsymbol{G}_{2} \langle \boldsymbol{C}, \boldsymbol{G}_{1} \otimes \boldsymbol{G}_{2} \rangle.$$

Stretches along G_F , F = 1, 2, 3 take the form:

(7.11)
$$\lambda_F = (\boldsymbol{g}_F \cdot \boldsymbol{g}_F)^{1/2} = \langle \boldsymbol{C}, \boldsymbol{A}_F \rangle^{1/2}.$$

and direction cosines between g_F , F = 1, 2, 3 can be expressed as follows:

(7.12)
$$\alpha_{FG} = (\boldsymbol{g}_F \cdot \boldsymbol{g}_G)(\lambda_F \lambda_G)^{-1}.$$

Finally, components $C_{FG} = \boldsymbol{g}_F \cdot \boldsymbol{g}_G$ in terms of λ_F and α_{FG} take the form:

(7.13)
$$C = \begin{bmatrix} \lambda_1^2 & \alpha_{12}\lambda_1\lambda_2 & \alpha_{13}\lambda_1\lambda_3 \\ \bullet & \lambda_2^2 & \alpha_{23}\lambda_2\lambda_3 \\ \bullet & \bullet & \lambda_3^2 \end{bmatrix}_{AB} \underline{\boldsymbol{G}}^A \otimes \underline{\boldsymbol{G}}^B.$$

We postulate a separate approximation of stretches along G_1 and G_2 :

(7.14)
$$\lambda_F = \tilde{\lambda}_F, \quad F = 1, 2.$$

We perform the change of variables: the Cauchy–Green tensor is expressed in terms of α_{FG} , $\tilde{\lambda}_1$, $\tilde{\lambda}_2$ and λ_3 :

(7.15)
$$\tilde{\boldsymbol{C}} = \tilde{\boldsymbol{C}}(\boldsymbol{C}, \tilde{\lambda}_1, \tilde{\lambda}_2) = \begin{bmatrix} \tilde{\lambda}_1^2 & \alpha_{12} \tilde{\lambda}_1 \tilde{\lambda}_2 & \alpha_{13} \tilde{\lambda}_1 \lambda_3 \\ \bullet & \tilde{\lambda}_2^2 & \alpha_{23} \tilde{\lambda}_2 \lambda_3 \\ \bullet & \bullet & \lambda_3^2 \end{bmatrix}_{AB} \underline{\boldsymbol{G}}^A \otimes \underline{\boldsymbol{G}}^B.$$

The augmented energy with the Lagrange multipliers $\tilde{\varrho}^1$, $\tilde{\varrho}^2$ corresponding to the constraints $\tilde{\lambda}_F = \lambda_F(C)$, F = 1, 2 take the following form:

(7.16)
$$\Psi = \tilde{\Psi}(\tilde{\boldsymbol{C}}, \tilde{\lambda}_1, \tilde{\lambda}_2; \boldsymbol{A}_1, \boldsymbol{A}_2) - \sum_{F=1}^2 \tilde{\varrho}^F [\tilde{\lambda}_F - \lambda_F(\boldsymbol{C})].$$

Since $\tilde{\boldsymbol{C}}(\boldsymbol{C}, \tilde{\lambda}_F) \equiv \boldsymbol{C}$ for $\tilde{\lambda}_F = \lambda_F$, F = 1, 2, we have:

(7.17)
$$\tilde{\Psi}(\tilde{\boldsymbol{C}}, \tilde{\lambda}_1, \tilde{\lambda}_2; \boldsymbol{A}_1, \boldsymbol{A}_2) = \Psi(\boldsymbol{C}; \boldsymbol{A}_1, \boldsymbol{A}_2).$$

The Clausius–Plank law $\frac{1}{2}\dot{\boldsymbol{C}}: \boldsymbol{S} - \dot{\Psi} = 0$, the assumptions above, and the Coleman–Noll procedure result in the following constitutive relations:

(7.18)
$$\begin{cases} \boldsymbol{S} = \sum_{F=1}^{2} \tilde{\varrho}^{F} \lambda_{F}^{-1} \boldsymbol{A}_{F} + \tilde{\boldsymbol{S}}, \\ \tilde{\boldsymbol{S}} = \tilde{\boldsymbol{P}} \left[2 \frac{\partial \tilde{\boldsymbol{\Psi}}}{\partial \tilde{\boldsymbol{C}}} \right], & \text{with } \tilde{\boldsymbol{P}} := \left[\frac{\partial \tilde{\boldsymbol{C}}}{\partial \boldsymbol{C}} \right]^{*}, \\ \tilde{\varrho}^{F} = \frac{\partial \tilde{\boldsymbol{\Psi}}}{\partial \tilde{\lambda}_{F}}. \end{cases}$$

A particular selection of the strain energy function Ψ follows the suggestions of Balzani *et al.* [35], and Simo and Pister [36]:

(7.19)
$$\begin{cases} \Psi = \widehat{\Psi}(C) + \widehat{\Psi}_{F}(\widetilde{\lambda}_{F}), \\ \widehat{\Psi} = \frac{1}{2}\Lambda[\ln \widetilde{J}]^{2} - \mu \ln(\widetilde{J}) + \frac{\mu}{2}(\widetilde{I}_{1} - 3) + \frac{1}{2}\Phi \sum_{F}(\widetilde{K}_{1,F} - 1)^{2}, \\ \widehat{\Psi}_{F}(\widetilde{\lambda}_{F}) = \frac{1}{2}\Gamma(\widetilde{\lambda}_{F}^{2} - 1)^{2}, \end{cases}$$

where $\tilde{K}_{1,F} = \tilde{I}_a - \tilde{\lambda}_F^2 \tilde{I}_1 + \tilde{I}_2$, $a = 2^F + 3$, and $\tilde{I}_a = I_a(\tilde{C})$, $a = 1, \dots 8$, μ is the shear modulus, and Λ , Φ , Γ are the material parameters.

A mixed Hu–Washizu type formulation takes into account the equilibrium, weak enforcement of separately approximated stretches $\tilde{\lambda}_F$, and weak enforcement of constitutive relation for $\tilde{\rho}^F$: find $\boldsymbol{u} \in \hat{\boldsymbol{u}} + V, \tilde{\lambda}_F \in Q, \tilde{\varrho}^F \in Q, F = 1, 2$ such that:

(7.20)
$$\begin{cases} \int_{\Omega} \frac{1}{2} (\boldsymbol{F}^T \boldsymbol{\nabla} \boldsymbol{v} + \boldsymbol{\nabla}^T \boldsymbol{v} \boldsymbol{F}) : \boldsymbol{S} \, dV = \int_{\Omega} \hat{\boldsymbol{b}} \cdot \boldsymbol{v} \, dV + \int_{\Gamma_N} \hat{\boldsymbol{t}} \cdot \boldsymbol{v} \, dS, \quad \forall \boldsymbol{v} \in V, \\ \int_{\Omega} (\lambda_F(\boldsymbol{C}) - \tilde{\lambda}_F) \delta \tilde{\varrho}^F \, dV = 0, \quad \forall \delta \tilde{\varrho}^F \in Q, \\ \int_{\Omega} (\tilde{\varrho}^F - \partial \tilde{\Psi} / \partial \tilde{\lambda}_F) \delta \tilde{\lambda}_F \, dV = 0, \quad \forall \delta \tilde{\lambda}_F \in Q. \end{cases}$$

The spaces V and Q and their finite element counterparts are the same as defined in Eqs. (2.11) and (2.12). Variables $\tilde{\lambda}_F$ and $\tilde{\varrho}^F$ can be eliminated at the element level by static condensation.

7.2. Numerical examples for anisotropic elasticity

In this section we present example solutions and the corresponding errors for bodies enforced by two families of fibres. We use the geometries identical as before though there are different properties of the medium and different loads. As before we are exclusively interested in the errors in displacements.

Pressurization of an anisotropic tube

We assume that the tube is enforced by the two families of fibres which constitute two helical spirals inclined at the angle of $\theta=64^{\circ}$ to the horizontal plane. The material data are as follows:

(7.21)
$$\mu = 10, \quad \Gamma = 1000, \quad \Lambda = 660.00, \quad \Phi = 10.$$

The internal pressure is p = 13.33. The characteristics of the solution: displacements u_z , u_r and the effective stress σ_0 , are presented in Fig. 14a–c. The error indicators corresponding to the three methods are displayed in Fig. 14d–f.

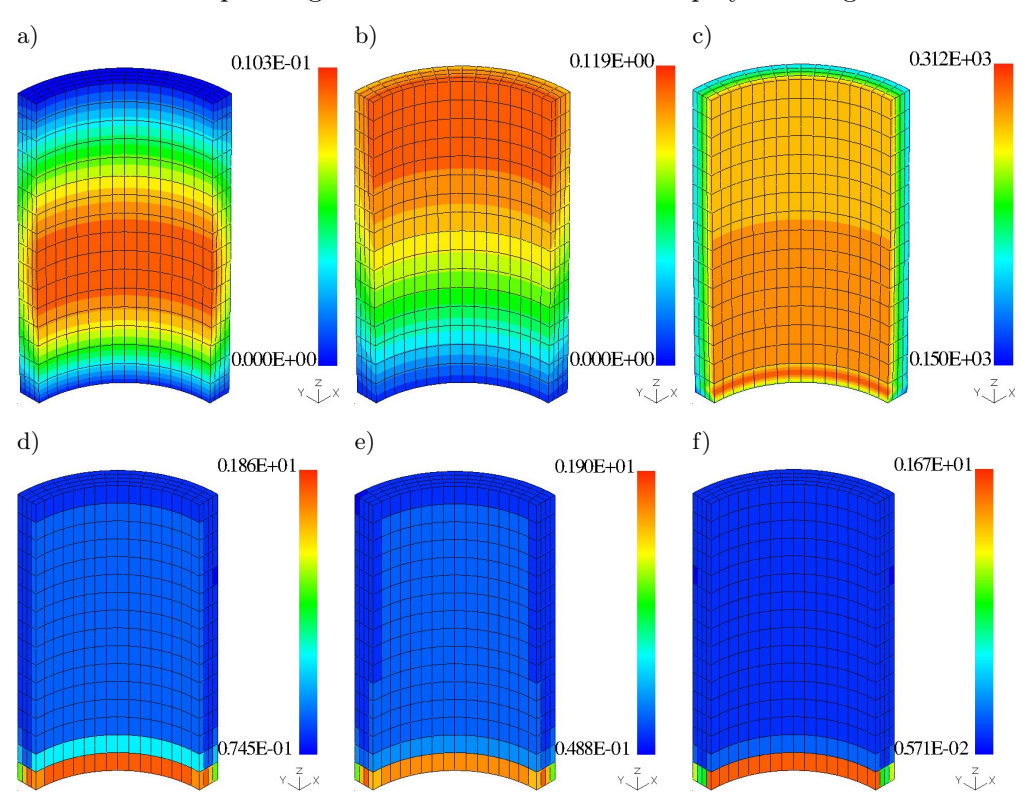


Fig. 14. Pressurization of a tube, anisotropic elasticity. Solution: a) u_z , b) u_r , c) σ_0 . Errors: d) Ainsworth/Oden, e) Ladevéze/Maunder, f) Demkowicz et al.

Bending of an anisotropic "tire tread"

In this case the fibres are located in the yz-plane (see the direction of axis below the color scale). They are inclined at the angle of $\theta = 45^{\circ}$ with respect

to the positive and negative y-axis, respectively. The material data are as in the previous example. The load acts on the upper surface in the y-direction, $\hat{t}_y = 0.5$.

In Fig. 15 we present the solution on the h-adaptive mesh with 2 levels of refinements. The solution characteristics include: displacements u_y , the effective stress σ_0 , and fibre tensions ρ_1 and ρ_2 . These figures seem to manifest the resistance of the fibres against the loading force. The distribution of error indicators is shown in Fig. 16. We can observe relative resemblance of the estimates, especially the two equilibration errors. The convergence is displayed in Fig. 17, where the H^1 -norm of the error was determined by comparing the current solutions with solutions found on meshes of the enriched order p=3.

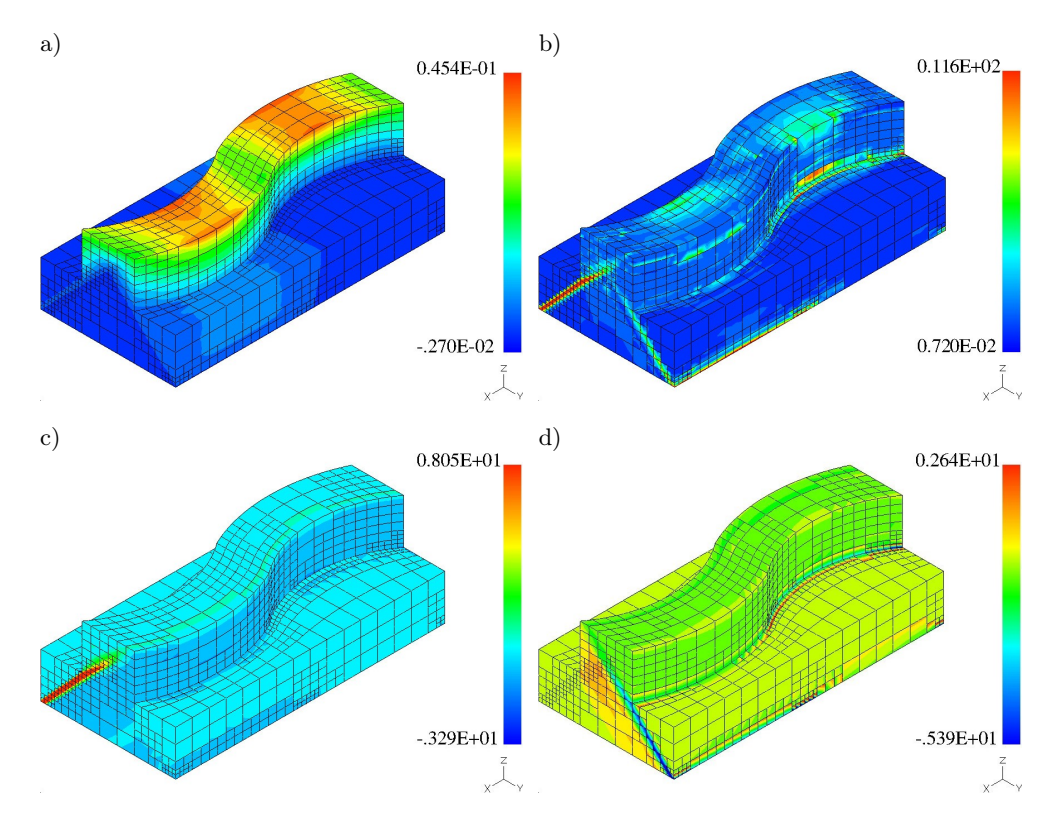


Fig. 15. "Tire tread", anisotropic elasticity. Solution on h-adaptive mesh: a) u_y , b) σ_0 , c) ρ_1 and d) ρ_2 .

Irregular tube with anisotropy

In our third example we put different enforcing fibres in two layers of the tube: we mimic the structure of an aorta with an internal layer called media and the external one – adventitia. Their thickness is $t_1 = 0.1685$ and $t_2 = 0.1033$.

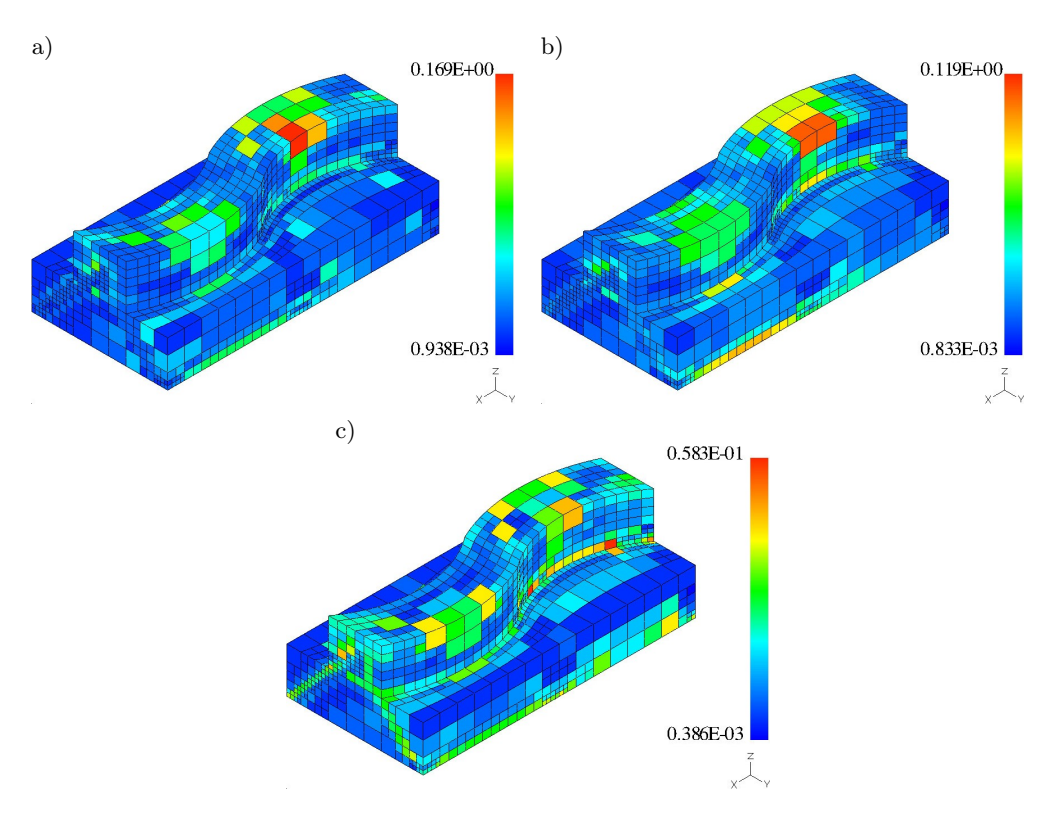


Fig. 16. "Tire tread", anisotropic elasticity. Errors: a) Ainsworth/Oden, b) Ladevéze/Maunder, c) Demkowicz et al.

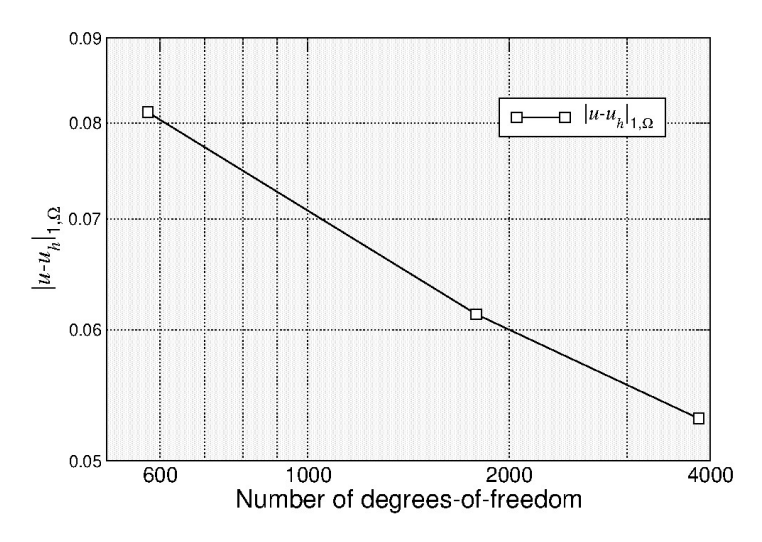


Fig. 17. Anisotropic "tire thread". Convergence of the H^1 -seminorm error for the h-adaptive meshes.

In the media the fibres constitute two helical spirals inclined at the angle of $\theta=20^{\circ}$ to the horizontal plane, in adventitia the spirals are inclined at the angle of $\theta=64^{\circ}$. The material data of the adventitia are such as in Eq. (7.21), while in media they are as follows:

(7.22)
$$\mu = 20, \quad \Gamma = 1000, \quad \Lambda = 653.33, \quad \Phi = 20.$$

Such data are typical for a rabbit carotid artery. The load of internal pressure is p = 13.33. The solution on an h-adaptive mesh with 3 levels of refinements is presented in Fig. 18, where displacements in the radial u_r and circumferential direction u_θ are displayed, and the effective stress σ_0 is shown.

In Fig. 19 we show the distribution of errors for the h-adaptive mesh. We can see better resemblance of equilibrated residual estimates than the remaining

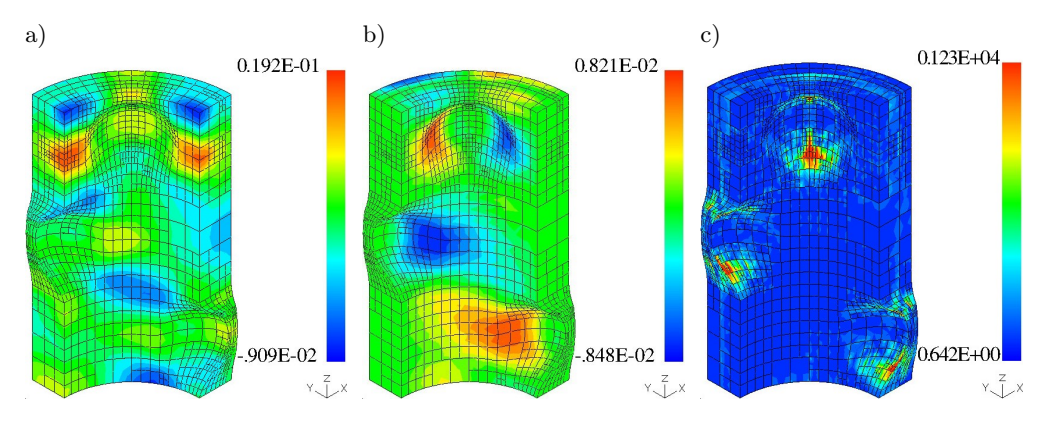


Fig. 18. Irregular tube, anisotropic elasticity. Solution on h-adaptive mesh: a) u_r , b) u_θ , c) σ_0 (on deformed configuration).

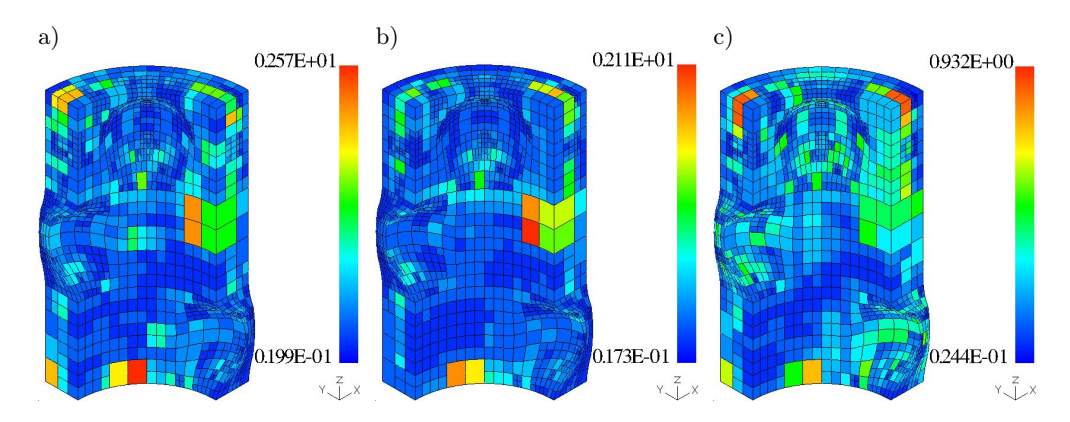


Fig. 19. Irregular tube, anisotropic elasticity. Errors on h-adaptive mesh:

a) Ainsworth/Oden,
b) Ladevéze/Maunder,
c) Demkowicz et al.

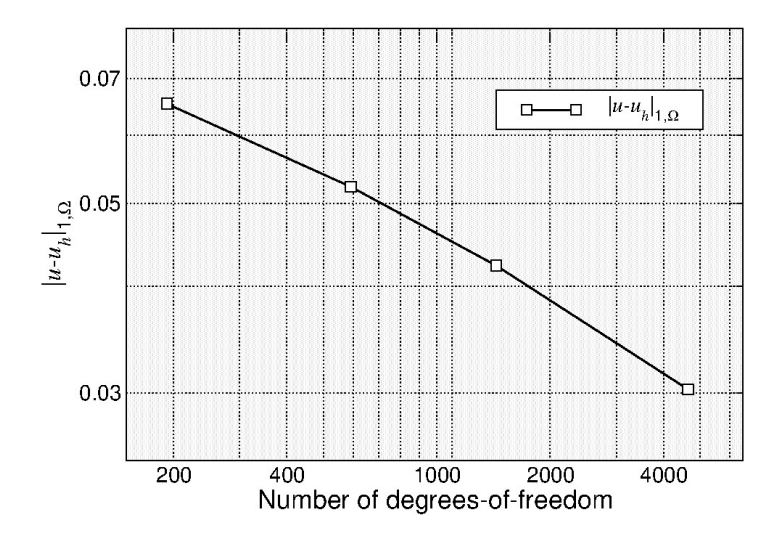


Fig. 20. Anisotropic irregular tube. Convergence of the H^1 -seminorm error for the h-adaptive meshes.

ones. We also present the convergence of the adaptive solutions in Fig. 20. The H^1 -seminorm error was found as in the previous examples.

8. Summary and conclusions

In this work we presented a study of applying the top-valued error estimation techniques for the finite element approximation of nonlinear elasticity. We investigated nearly incompressible media and anisotropic solids enforced by 2 families of fibres. Both problems require the mixed formulations to maintain stability.

The error estimation methods included the element residual implicit method of Demkowicz et al. [26], also proposed by Bank and Weiser [34], and the method of self-equilibrated residuals due to Ainsworth and Oden [18]. The last algorithm was investigated with two versions of self-equilibration procedures: the one invented by Ainsworth and Oden [27] and the approach due to Ladevéze and Maunder [19]. The error estimates procedures work for general grids of hexahedral elements. They allow for, so called, 1-irregular meshes which result from selective refinement of elements. We presented the details necessary for generalisation of the Ladevéze and Maunder method for 1-irregular meshes in 3D.

Our numerical experiments indicate that the three methods of error estimation result in very close error indicators for the initial, regular meshes for isotropic problems. This similarity deteriorates a little for 1-irregular meshes. Such conclusion seems not to be true for anisotropic elasticity. In this case we observe that the element residual method results in estimates which are less

similar than both self-equilibrated residual procedures. One might suspect that the anisotropic solutions are much tougher to approximate.

Appendix A

The coefficient of correlation is defined as follows:

(A.1)
$$\rho_{xy} = \frac{1}{n} \sum_{i=1}^{n} \frac{(x_i - \bar{x})(y_i - \bar{y})}{S_x S_y},$$

where \bar{x} and \bar{y} the average values of variables x_i and y_i :

(A.2)
$$\bar{x} = \frac{1}{n} \sum_{i=1}^{n} x_i, \quad \bar{y} = \frac{1}{n} \sum_{i=1}^{n} y_i,$$

and S_x and S_y are the standard deviations:

(A.3)
$$S_x^2 = \frac{1}{n} \sum_{i=1}^n (x_i - \bar{x})^2, \quad S_y^2 = \frac{1}{n} \sum_{i=1}^n (y_i - \bar{y})^2.$$

Below we present the tables of correlation coefficients for subsequent pairs of error estimation techniques, and for different meshes (denoted as h0-the initial mesh, h1-adaptive mesh of 1st level, etc.).

Let us denote the element error indicators $\eta_i^{A/O}$ of Ainsworth/Oden, $\eta_i^{L/M}$ of Ladevéze/Maunder, and $\eta_i^{D/B}$ of Demkowicz *et al.* (and Bank/Weiser), where *i* is the element number, $i=1,\ldots,n$, and *n* is the number of elements in the mesh. Then in Tables 1 and 3 we have:

in the first column: $x_i = \eta_i^{A/O}$, $y_i = \eta_i^{L/M}$, correlation is listed, in the second column: $x_i = \eta_i^{A/O}$, $y_i = \eta_i^{D/B}$, correlation is listed, in the third column: $x_i = \eta_i^{D/B}$, $y_i = \eta_i^{L/M}$, correlation is listed.

Table 1. Correlation between the errors, isotropic elasticity.

Problem	Mesh	Ainsworth/Oden Ladevéze/Maunder	Ainsworth/Oden Demkowicz et al.	$\begin{array}{c} {\rm Demkowicz}\ et\ al. \\ {\rm Ladev\'eze/Maunder} \end{array}$	
Tube straight	h0	0.99	0.95	0.94	
"Tire tread"	h0	0.99	0.89	0.89	
	h1	0.96	0.75	0.83	
	h2	0.93	0.57	0.72	
Tube irregular	h0	0.96	0.89	0.88	
	h1	0.87	0.64	0.82	
	h2	0.93	0.70	0.77	
	h3	0.91	0.67	0.74	

Problem	Mesh	Ainsworth/Oden		Ladevéze/Maunder		Demkowicz et al.	
		error ind.	eff. index	error ind.	eff. index	error ind.	eff. index
Tube straight	h0	2.98e-3	2.51e-2	3.20e-3	2.04e-2	3.20e-3	2.02e-2
"Tire tread"	h0	1.78e-4	12.26e-3	3.07e-4	2.49e-3	3.04e-4	2.43e-3
	h1	1.97e-4	2.20e-3	2.34e-4	2.60e-3	2.37e-4	2.63e-3
	h2	1.50e-4	2.22e-3	2.33-4	2.60e-3	1.77e-4	2.64e-3
Tube irregular	h0	1.69e-4	1.86e-3	1.82e-4	2.01e-2	8.48e-5	9.38e-3
	h1	7.56e-5	1.48e-2	7.96e-5	1.56e-2	1.33e-5	2.62e-3
	h2	1.26e-4	4.32e-2	1.19e-4	4.07e-2	1.79e-5	1.63e-2
	h3	4.20e-5	2.64e-2	4.42e-5	2.78e-2	2.40e-6	1.51e-3

Table 2. Error indicators and effectivity indices, isotropic elasticity.

Table 3. Correlation between the errors, anisotropic elasticity.

Problem	Mesh	Ainsworth/Oden Ladevéze/Maunder	Ainsworth/Oden Demkowicz et al.	Demkowicz <i>et al.</i> Ladevéze/Maunder	
Tube straight	h0 0.99		0.94	0.94	
"Tire tread"	h0	0.90	0.71	0.68	
	h1	0.84	0.66	0.63	
	h2	0.85	0.65	0.64	
Tube irregular	h0	0.60	0.49	0.47	
	h1	0.73	0.61	0.46	
	h2	0.78	0.62	0.52	
	h3	0.81	0.55	0.44	

For the 2 sets of quantities correlation becomes 1 if they grow linearly together, correlation is 0 if they are not correlated (they fill uniformly a circle on a 2D plane, for instance). So the closer coefficient of correlation is to 1, the closer two error estimates are indication of elements with the larger error which should be a subject of adaptation.

We note excellent correlation for initial meshes (h0) and some deterioration for adaptive meshes. In general it is quite satisfactory.

For strongly anisotropic elasticity we observe good correlation between the self-equilibrating residuals estimates (with different techniques for the equilibrating algorithm). Moreover, it grows with the level of refinements. The correlation is much lower considering the Demkowicz *et al.* method. It suggests that these problems are much more difficult to approximate and adequate refinement is needed to reach the asymptotic behaviour, and that the simple residual technique does not cope with such problems very well.

In Tables 2 and 4 we collected global error indicators and estimated effectivity indices which are evaluated by comparing the solutions on the actual meshes with

Problem	Mesh	Ainsworth/Oden		Ladevéze/Maunder		Demkowicz et al.	
		error ind.	eff. index	error ind.	eff. index	error ind.	eff. index
Tube straight	h0	$5.23e{+1}$	6.75e + 3	$4.94e{+1}$	$6.23e{+3}$	$5.33e{+1}$	6.72e + 3
"Tire tread"	h0	$1.65e{+0}$	20.3e+0	$1.86\mathrm{e}{+0}$	$2.30e{+1}$	1.03e+0	$2.50e{+1}$
	h1	1.42e+0	$2.32e{+1}$	1.82e + 0	$2.97e{+1}$	2.14e+0	$3.47e{+1}$
	h2	$1.05 e{+0}$	$1.98e{+1}$	1.37e + 0	$2.57e{+1}$	$1.68e{+1}$	$3.17e{+1}$
Tube irregular	h0	$6.50e{+1}$	$9.95e{+2}$	$3.56\mathrm{e}{+1}$	$5.46e{+2}$	$6.26\mathrm{e}{+1}$	$8.56\mathrm{e}{+1}$
	h1	$2.86e{+1}$	5.47e + 2	$3.56\mathrm{e}{+1}$	$5.46e{+2}$	$526e{+1}$	$9.58e{+2}$
	h2	$4.20e{+1}$	$9.95e{+2}$	$3.17e{+1}$	7.52e+2	$1.95\mathrm{e}{+1}$	$4.65\mathrm{e}{+2}$
	h3	9.74e + 0	3.22e+2	9.77e + 0	3.22e+2	3.35e+0	$1.17\mathrm{e}{+2}$

Table 4. Error indicators and effectivity indices, anisotropic elasticity.

solutions on enriched meshes to p=3. We observe that the effectivity indices depend on the problem being considered as it is anticipated by the paper of Brink and Stein [23].

Appendix B. Constrained approximation

We consider a basis of polynomials $\Phi_i(\xi)$, i = 1, ..., p + 1 of the order p on a unit domain [0,1] which with appropriate numbering satisfy the conditions: $\Phi_1(0) = 1$, $\Phi_1(1) = 0$ and $\Phi_2(0) = 0$, $\Phi_2(1) = 1$, and the remaining vanish in $\xi = 0$ and $\xi = 1$. The restriction of such polynomials to $\xi \in [0, 1/2]$ can be expressed by the same basis $\phi_i(\xi) = \Phi_i(\xi)$, i = 1, ..., p + 1 with a nonsingular matrix $\{r_{ij}\}_{i,j=1}^{p+1}$ as they span the same space:

(B.1)
$$\Phi_i(\xi/2) = \sum_{j=1}^{p+1} r_{ij}\phi_j(\xi), \quad \xi \in [0, 1].$$

The matrix r_{ij} depends solely on the selected kind of polynomials. It could be found, for instance, by demanding satisfaction of Eq. (B.1) at p + 1 distinct points in the interval $\xi \in [0, 1]$.

We consider the shape functions of hexahedral element as a tensor product of 1D polynomials Φ_i :

(B.2)
$$\Psi_{ijk}(\xi_1, \xi_2, \xi_3) = \Psi_i(\xi_1) \cdot \Psi_j(\xi_2) \cdot \Psi_k(\xi_3),$$
$$i, j, k \in 1, \dots, p+1, \, \xi_1, \xi_2, \xi_3 \in [0, 1].$$

Now let us consider a 3D situation depicted in Fig. 21, where the smaller hexahedral element of the size 1/2 is adjacent to its larger neighbor – the hexahedral element of the dimension 1. Assume that the common side of the smaller element occupies the quarter $[0, 1/2]^2$ of the larger element.

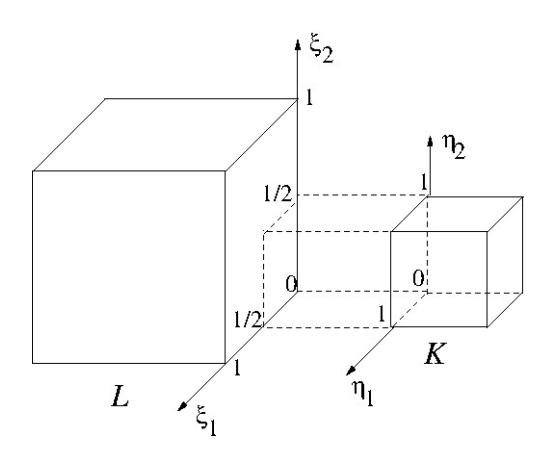


Fig. 21. Smaller neighbor K constrained by the larger element L through the common side; $\eta_1 = 2\xi_1, \ \eta_2 = 2\xi_2.$

Now we consider the shape functions of both elements restricted to the common side. They can be expressed as:

(B.3)
$$\Psi_{ij}(\xi_1, \xi_2) = \Phi_i(\xi_1) \cdot \Phi_j(\xi_2), \\ \psi_{ij}(\eta_1, \eta_2) = \phi_i(\eta_1) \cdot \phi_j(\eta_2).$$

According to (B.1) we can express Ψ_{ij} as follows:

(B.4)
$$\Psi_{ij} = \sum_{k=1}^{p+1} \sum_{l=1}^{p+1} (r_{ik}\phi_k \cdot r_{jl}\phi_l) = \sum_{k=1}^{p+1} \sum_{l=1}^{p+1} (r_{ik}r_{jl} \cdot \phi_k\phi_l).$$

Introducing numbering with single indices:

(B.5)
$$I = (i-1) \cdot (p+1) + j, \quad K = (k-1) \cdot (p+1) + l,$$

and notation:

$$(B.6) r_{ik}r_{jl} = R_{IJ},$$

we can write

(B.7)
$$\Psi_I = \sum_{J=1}^{(p+1)^2} R_{IJ} \psi_J.$$

Analogous relations can be established between the edge functions of elements L and K depicted in Fig. 22, though involving directly Eq. (B.1).

We can collect the formula like (B.7) for all faces (and edges) of the small element adjacent to its larger neighbors, and in this way express the functions Ψ_I which match the functions of the larger neighbors. It turns out that some of such

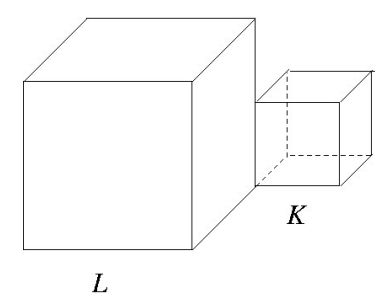


Fig. 22. Smaller neighbor K constrained by the larger element L through the common edge.

equations are redundant (appear more than once), so they must be eliminated. In this way we obtain the formula (5.1a). The relation for the dofs (5.1b) is obtained keeping in mind that dofs are the dual functionals to shape functions (Ciarlet [37]), so they can be expressed by the transpose matrix. Actually, the latter relations can be written in the form avoiding the mentioned above redundancy, in a closed formula:

(B.8)
$$u_k = \sum_{i=1}^{NC(k)} U_{L(i,k)} R_{ik}, \quad k = 1, \dots, \text{ndofs},$$

where, ndofs is a number of degrees-of-freedom of the smaller element, NC(k) is a number of dofs of larger neighbors constraining dof u_k , L(i, k) stands for indices of these constraining dof, i = 1, ..., NC(k). The algorithm expressing (B.8), and its transpose version for shape functions has the form as in Fig. 23.

```
\begin{array}{lll} u_k = 0, \ k = 1, \dots, \mathrm{ndof} & \Psi_i = 0, \ i = 1, \dots, \mathrm{ndof} \\ \text{for } k = 1, \dots, \mathrm{ndof} & \text{for } k = 1, \dots, \mathrm{ndof} \\ \text{for } i = 1, NC(k) & \text{for } i = 1, \dots, NC(k) \\ & u_k := u_k + U_{L(i,k)} R_{ik} & \Psi_{L(i,k)} := \Psi_{L(i,k)} + R_{ik} \psi_k \\ \text{endfor } i & \text{endfor } i \end{array}
```

Fig. 23. Algorithms for evaluating unconstrained dofs u_k and constrained shape functions Ψ_i .

References

- I. Babuška, B. Andersson, The splitting method as a tool for multiple damage analysis, SIAM Journal on Scientific Computing, 26, 1114–1145, 2005.
- B. Andersson, J. Greer Jr., Creation and verification of world's Largest k_i-databases for multiple cracks at countersunk and straight-shank hole in a plate subject to tension, bending and in-loading, [in:] ICAF, 29-th Symposium Nagoya, Japan, 7-9 June, Committee for Aeronautical Fatigue ICAF, 2017.

- 3. B. Andersson, U. Falk, I. Babuška, T. Von Petersdorff, Reliable stress and fracture mechanics analysis of complex components using a h-p version of FEM, International Journal for Numerical Methods in Engineering, 38, 13, 2135–2163, 1995.
- 4. A. Zdunek, Tests with FALKSOL. A massively parallel multi-level domain decomposing direct solver, Computers and Mathematics with Applications, 97, 207–222, 2021.
- 5. B. Andersson, U. Falk, Large-scale FE-analysis for reliable verification and validation: the GDF challenge, Book chapter prepared for the docomentation of the achievements in the EU FP7 MAAXIMIS project, private communication, 20 pp.
- 6. MAAXIMUS. More Affordable Aircraft structure through eXtended, Integrated, and Mature nUmerical Sizing, 2008–2016, EU FP-7 Transport, Final report summary, accessed 29.11.2024, https://cordis.europa.eu/docs/results/213/213371/final1-maaximus-final-report-publishable-summary-uploaded.pdf.
- A. ERIKSSON, C. PACOSTE, A. ZDUNEK, Numerical analysis of complex instability behaviour using incremental-iterative strategies, Computer Methods in Applied Mechanics and Engineering, 179, 3, 265–305, 1999.
- 8. A. ZDUNEK, W. RACHOWICZ, A mixed finite element formulation for compressible finite hyperelasticity with two fibre family reinforcement, Computer Methods in Applied Mechanics and Engineering, 345, 233–262, 2019.
- P.R. AMESTOY, I.S. DUFF, J.-Y. L'EXCELLENT, Multifrontal parallel distributed symmetric and unsymmetric solvers, Computer Methods in Applied Mechanics and Engineering, 184, 2, 501–520, 2000.
- P.R. AMESTOY, I.S. DUFF, J.-Y. L'EXCELLENT, J. KOSTER, A fully asynchronous multifrontal solver using distributed dynamic scheduling, SIAM Journal on Matrix Analysis and Applications, 23, 1, 15–41, 2001
- 11. P.R. AMESTOY, A. GUERMOUCHE, J.-Y. L'EXCELLENT, S. PRALET, Hybrid scheduling for the parallel solution of linear systems, Parallel Computing, 32, 2, 136–156, 2006, Parallel Matrix Algorithms and Applications (PMAA'04).
- 12. L. Demkowicz, Computing with hp-adaptive finite elements: Volume 1, One and Two Dimensional Elliptic and Maxwell Problems, 1st ed., Chapman and Hall/CRC, New York, 2006.
- 13. L. Demkowicz, J. Kurtz, D. Pardo, M. Paszyński, W. Rachowicz, A. Zdunek, Computing with Hp-Adaptive Finite Elements: Volume 2, Frontiers: Three Dimensional Elliptic and Maxwell Problems with Applications, Chapman and Hall/CRC, 2008.
- M. AINSWORTH, J.T. ODEN, A Posteriori Error Estimation in Finite Element Analysis, John Wiley and Sons, 2000.
- E. STEIN, M. RÜTER, Finite Element Methods for Elasticity with Error-Controlled Discretization and Model Adaptivity, John Wiley and Sons, pp. 1–96, 2017.
- R. Verfürth, A Posteriori Error Estimation Techniques for Finite Element Methods, Oxford University Press, 2013.
- L. Chamoin, F. Legoll, An introductory review on a posteriori error estimation in finite element computations, Society of Industrial and Applied Mathematics Review, 65, 4, 963–1028, 2023.

- 18. A. AINSWORTH, J.T. ODEN, A unified approach to a posteriori error estimation using element residual methods, Numerische Mathematik, 65, 23–50, 1993.
- P. LADEVÉZE, E.A.W. MAUNDER, A general method for recovering equilibrating element tractions, Computer Methods in Applied Mechanics and Engineering, 137, 2, 111–151, 1996.
- W. Rachowicz, Evaluation and comparison of residual error esimates with selfequilibrated fluxes in three dimensions, [in:] ECCM-2001: 2nd European Conference on Computational Mechanics: Solids, Structures and Coupled Problems in Engineering, Cracow, Poland, June 26–29, 2001.
- A. ZDUNEK, W. RACHOWICZ, Application of the hp-adaptive finite element method to the three-dimensiona scattering of time-harmonic electromagnetic waves, [in:] ECCM-2001: 2nd European Conference on Computational Mechanics: Solids, Structures and Coupled Problems in Engineering, Cracow, Poland, June 26–29, 2001.
- 22. G. ZBOIŃSKI, Adaptive hpq finite element methods for the analysis of 3D-based models of complex structures. Part 2. A posteriori error estimation, Computer Methods in Applied Mechanics and Engineering, 267, 531–565, 2013.
- U. Brink, E. Stein, A posteriori error estimation in large-strain elasticity using equilibrated local Neumann problems, Computer Methods in Applied Mechanics and Engineering, 161, 1, 77–101, 1998.
- 24. M. RÜTER, E. STEIN, Analysis, finite element computation and error estimation in transversely isotropic nearly incompressible finite elasticity, Computer Methods in Applied Mechanics and Engineering, 190, 5, 519–541, 2000.
- A. ZDUNEK, W. RACHOWICZ, A 3-field formulation for strongly transversely isotropic compressible finite hyperelasticity, Computer Methods in Applied Mechanics and Engineering, 315, 478–500, 2017.
- L. Demkowicz, J.T. Oden, T. Strouboulis, Adaptive finite elements for flow problems with moving boundaries. Part I: Variational principles and a posteriori estimates, Computer Methods in Applied Mechanics and Engineering, 46, 2, 217–251, 1984.
- A. AINSWORTH, J.T. ODEN, A posteriori error estimators for second order elliptic systems. Part 2. An optimal order process for calculating self-equilibrating fluxes, Computers and Mathematics with Applications, 26, 75–87, 1993.
- 28. J. Badger, S. Henneking, S. Petrides, L. Demkowicz, Scalable DPG multigrid solver for Helmholtz problems: A study on convergence, Computers and Mathematics with Applications, 148, 81–92, 2023.
- 29. M. Ainsworth, J.T. Oden, A posteriori error estimation in finite element analysis, Computer Methods in Applied Mechanics and Engineering, 142, 1, 1–88, 1997.
- R.J. FLORY, Thermodynamic relations for highly elastic materials, Transactions of the Faraday Society, 57, 829–838, 1961.
- 31. J.C. Simo, R.L. Taylor, K.S. Pister, Variational and projection methods for the volume constraint in finite deformation elasto-plasticity, Computer Methods in Applied Mechanics and Engineering, 51, 1, 177–208, 1985.
- I. Babuška, W.C. Rheinbolt, Error estimates for adaptive finite element computations, Society of Industrial and Applied Mathematics Journal on Numerical Analysis, 15, 4, 736– 754, 1978.

- 33. L. Demkowicz, T.J. Oden, W. Rachowicz, O. Hardy, Toward a universal h-p adaptive finite element strategy, Part 1. Constrained approximation and data structure, Computer Methods in Applied Mechanics and Engineering, 77, 79–112, 1989.
- 34. R.E. Bank, A. Weiser, Some a posteriori error estimators for elliptic partial differential equations, Mathematical Computation, 44, 283–301, 1985.
- 35. D. Balzani, P. Neff, J. Schröder, G.A. Holzapfel, *A polyconvex framework for soft biological tissues, adjustment to experimental data*, International Journal of Solids and Structures, **43**, 6052–6070, 2006.
- J.C. Simo, K.S. Pister, Remarks on rate constitutive equations for finite deformation, Computer Methods in Applied Mechanics and Engineering, 46, 201–215, 1984.
- P.G. CIARLET, The Finite Element Method for Elliptic Problems, North-Holland Publishing Company, 1978.

Received November 30, 2024; revised version April 16, 2025.

Published online August 6, 2025.